INVESTIGATION OF THE RAYLEIGH CRITICAL ANGLE PHENOMENON FOR THE CHARACTERIZATION OF SURFACE PROPERTIES PHASE II

A TECHNICAL REPORT

30 September 1982

Prepared For:

Air Force Office of Scientific Research
Bolling Air Force Base
Washington, D.C. 20332

SPECTRON DEVELOPMENT LABORATORIES INC.

UNCLASSIFIED

SECURITY CLASSIFICATION OF THIS PAGE (When Data Entered)

REPORT DOCUMENTATION PAGE		READ INSTRUCTIONS BEFORE COMPLETING FORM
1. REPORT NUMBER AFOSR-TR- 82-1061	2. GOVT ACCESSION NO. AD-A123 145	3. RECIPIENT'S CATALOG NUMBER
4. TITLE (and Subtitle) INVESTIGATION OF THE RAYLEIGH CRITICAL ANGLE PHENOMENON FOR THE CHARACTERIZATION OF SURFACE PROPERTIES PHASE II		5. TYPE OF REPORT & PERIOD COVERED Interim 01 JUL 82 to 30 SEP 82 6. PERFORMING ORG. REPORT NUMBER
7. AUTHOR(s) B. P. Hildebrand, G.L. Fitzpatrick, A.J. Boland		8. CONTRACT OR GRANT NUMBER(s) F49620-81-C-0040
9. PERFORMING ORGANIZATION NAME AND ADDRESS Spectron Development Laboratories, Inc. 3303 Harbor Blvd., Suite G-3 Costa Mesa, CA 92626		10. PROGRAM ELEMENT, PROJECT, TASK AREA & WORK UNIT NUMBERS 2306/A2 61102F
11. CONTROLLING OFFICE NAME AND ADDRESS Air Force Office of Scientific Research Building #410 Bolling AFB, Washington, DC 20332		12. REPORT DATE 30 September 1982 13. NUMBER OF PAGES 56
14. MONITORING AGENCY NAME & ADDRESS(if different from Controlling Office)		15. SECURITY CLASS. (of this report) UNCLASSIFIED 15a. DECLASSIFICATION/DOWNGRADING SCHEDULE

16. DISTRIBUTION STATEMENT (of this Report)

Approved for public release;
distribution unlimited.

17. DISTRIBUTION STATEMENT (of the abstract entered in Block 20, if different from Report)

18. SUPPLEMENTARY NOTES

19. KEY WORDS (Continue on reverse side if necessary and identify by block number)

20. ABSTRACT (Continue on reverse side if necessary and identify by block number)

A series of experiments on single crystals and other materials of a controlled nature have been performed. These experiments have provided strong constraints on the interpretation of critical angle measurements made with an apparatus which employs a focused acoustic source rather than a plane wave source. Certain "anomalous" measurements reported earlier on uncontrolled materials have been seen again in these controlled materials. Because of the known angular periodicity of the material properties (angle of rotation about certain symmetry

OVER

DD FORM 1 JAN 73 1473 EDITION OF 1 NOV 65 IS OBSOLETE

UNCLASSIFIED

SECURITY CLASSIFICATION OF THIS PAGE (When Data Entered)

axes of a crystal, for example), it has been shown that these effects are dependent on the sample and much less dependent on the nature and details of the experimental apparatus. Nevertheless, a focused acoustic source could produce a number of effects that would not be expected if plane wave excitation of surface waves were employed. Accordingly, theoretical and experimental studies designed to determine what these effects may be has been started.

INVESTIGATION OF THE RAYLEIGH CRITICAL ANGLE PHENOMENON FOR THE CHARACTERIZATION OF SURFACE PROPERTIES

PHASE II

A Technical Report
30 September 1982
SDL No. 82-2188-11TR

Accession For	
NTIS GRA&I	☒
DTIC TAB	☐
Unannounced	☐
Justification	
By	
Distribution/	
Availability Codes	
Dist	Avail and/or Special
A	

Principal Investigator
B. P. Hildebrand

Senior Scientist
G. L. Fitzpatrick

Computer Scientist
A. J. Boland

Sponsored by:

Advanced Research Projects Agency (DOD)
ARPA Order No. 4109
Monitored by AFOSR under Contract #F49620-81-C-0040

SPECTRON DEVELOPMENT LABORATORIES INC.
3303 Harbor Boulevard, Suite G-3
Costa Mesa, California 92626 (714) 549-8477

TABLE OF CONTENTS

LIST OF FIGURES

LIST OF FIGURES (CON'T)

1.0 INTRODUCTION

During this quarter we performed a series of experiments on single crystals and other materials of a controlled nature. These experiments have provided strong constraints on the interpretation of critical angle measurements made with an apparatus which employs a focused acoustic source rather than a plane wave source. Certain "anomalous" measurements reported earlier on uncontrolled materials have been seen again in these controlled materials. Because of the known angular periodicity of the material properties (angle of rotation about certain symmetry axes of a crystal, for example), we have been able to show that these effects are dependent on the sample and much less dependent on the nature and details of the experimental apparatus.

Nevertheless, a focused acoustic source could produce a number of effects that would not be expected if plane wave excitation of surface waves were employed. Accordingly, we have begun theoretical and experimental studies designed to determine what these effects may be.

2.0 QUALITATIVE ANALYSIS OF THE EFFECT OF CONVERGING BEAMS

A cursory description of our apparatus has been given in previous reports. However, the influence our unique geometry has upon the experimental results has not been fully assessed. In this section we provide an initial analysis of our experiment based upon well known optics and acoustics theory. Subsequent reports will elaborate further.

2.1 Plane of Incidence

In order to obtain high resolution critical angle images as described in our initial proposal, we chose the geometry shown in Fig. 1. The transmitter crystal is followed by a lens which focuses the sound to a point at the center of rotation of the goniometer. The sample is placed with its surface also at the center of rotation, and its surface normal in the plane of the goniometer. The receiving transducer consists of a very small element placed on the other arm of the goniometer. The central ray of the transmitter, and the receiver fulfill the specular reflecting geometry.

The experiment is performed by energizing the transmitter with a continuous sine wave at the appropriate frequency and monitoring the receiver with a vector volt meter. The sample is placed in the x-y plane and the goniometer carrying the transducers is moved from a small angle to a large one or vice versa. In this process, the transducers pass through all three critical angles, θ_L, θ_S, θ_R (longitudinal, transverse, and Rayleigh, respectively). The complex reflectivity as a function of angle is the recorded variable.

In the past, this type of experiment has been performed with large transducers and plane waves. Therefore, each of the critical angles mentioned above was interrogated separately, except perhaps for θ_S and θ_R which lie quite close together for some materials. In our geometry, the focused cone can sometimes contain all three critical angles.

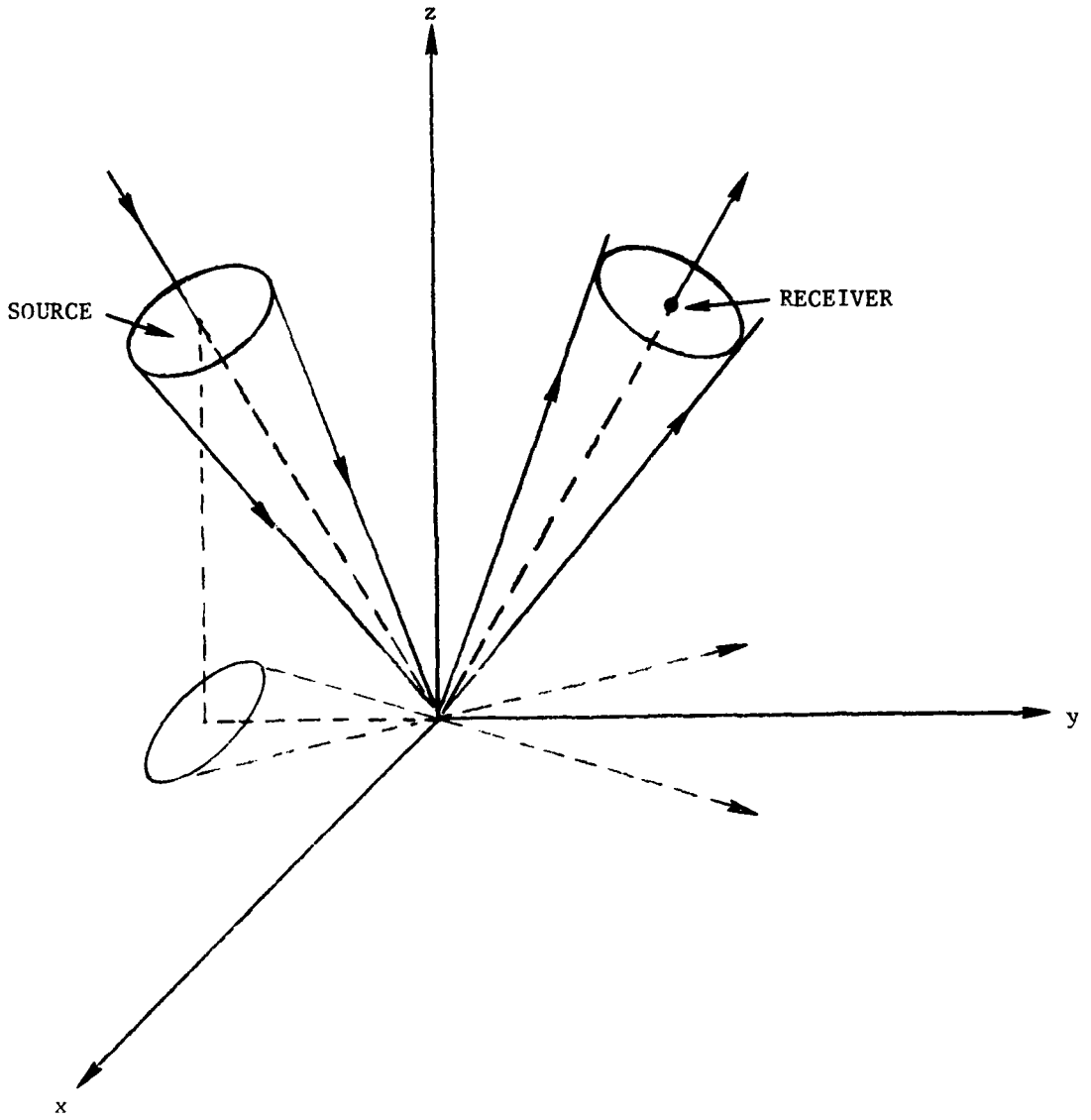

Fig. 1. Isometric sketch of the experimental system.

Therefore, in addition to the Rayleigh surface wave, there may be lateral waves which then reradiate to form head waves that will be seen by the receiver. For our usual geometry, a 25 mm transmitter is focused at 100 mm resulting in a converging cone of 14.25° included angle. In aluminum, for example, θ_L = 13° 26', θ_T = 29° 20' and θ_R = 31° 36'. Hence, θ_L and θ_S could not be encompassed simultaneously although a slightly larger transducer could. θ_S and θ_R are, however, always energized together. Thus, a Rayleigh and transverse lateral wave will be present simultaneously. Both of these waves will generate head waves in the water which will be seen by the receiver.

The theory, for the reflectivity of a surface and the various waves generated, is admirably summarized by Überall.[1] We will repeat it here as a foundation for further exposition. The general situation of a point source in a liquid half space in contact with an isotropic solid is shown in Fig. 2. The resulting waves are:

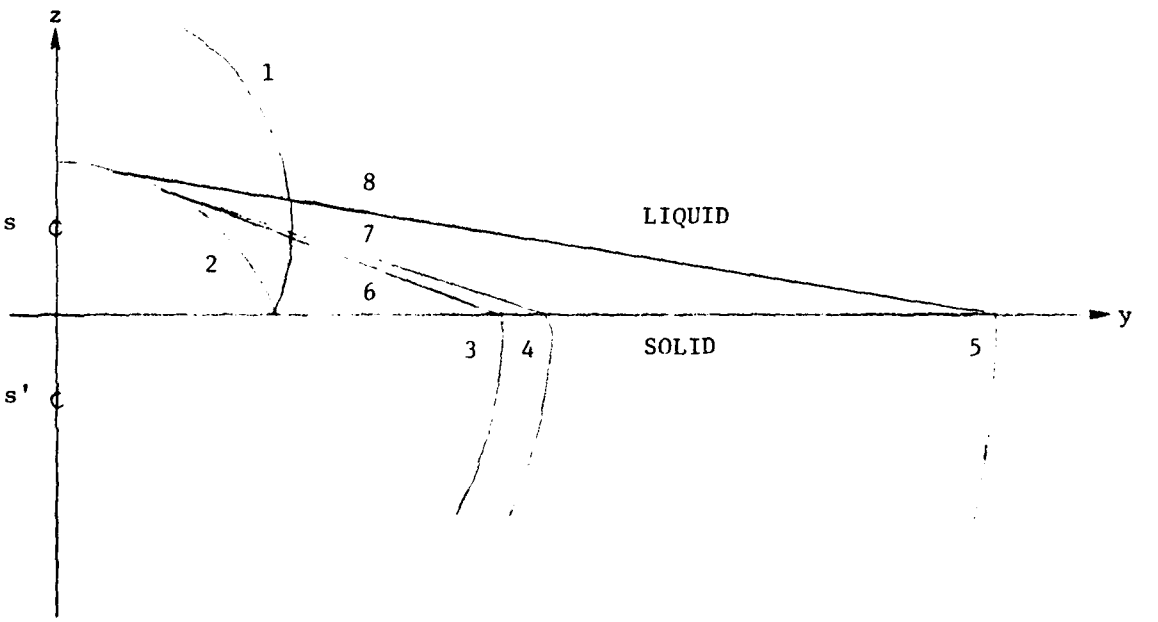

Fig. 2. Side view of wave fronts generated by a point source in the liquid. The solid is isotropic.

1. Wave front propagated from the source, S.
2. Wave front reflected by the surface (virtual source, S').
3. Rayleigh (generalized) surface wave with amplitude falling off in the solid, traveling at velocity, C_R.
4. Lateral surface wave traveling at shear velocity, C_S.
5. Lateral surface wave traveling at compressional velocity, C_L.
6. Head wave generated by the Rayleigh wave.
7. Head wave generated by the shear lateral wave.
8. Head wave generated by the compressional lateral wave.

The amplitudes and phases of all of these waves can be calculated theoretically. Since the source is a point, the head waves will be conical.

This geometry is closely related to the one that we have chosen. If we consider our source to be at the focus of our lens and restrict the cone of rays, we have the situation shown in Fig. 3.

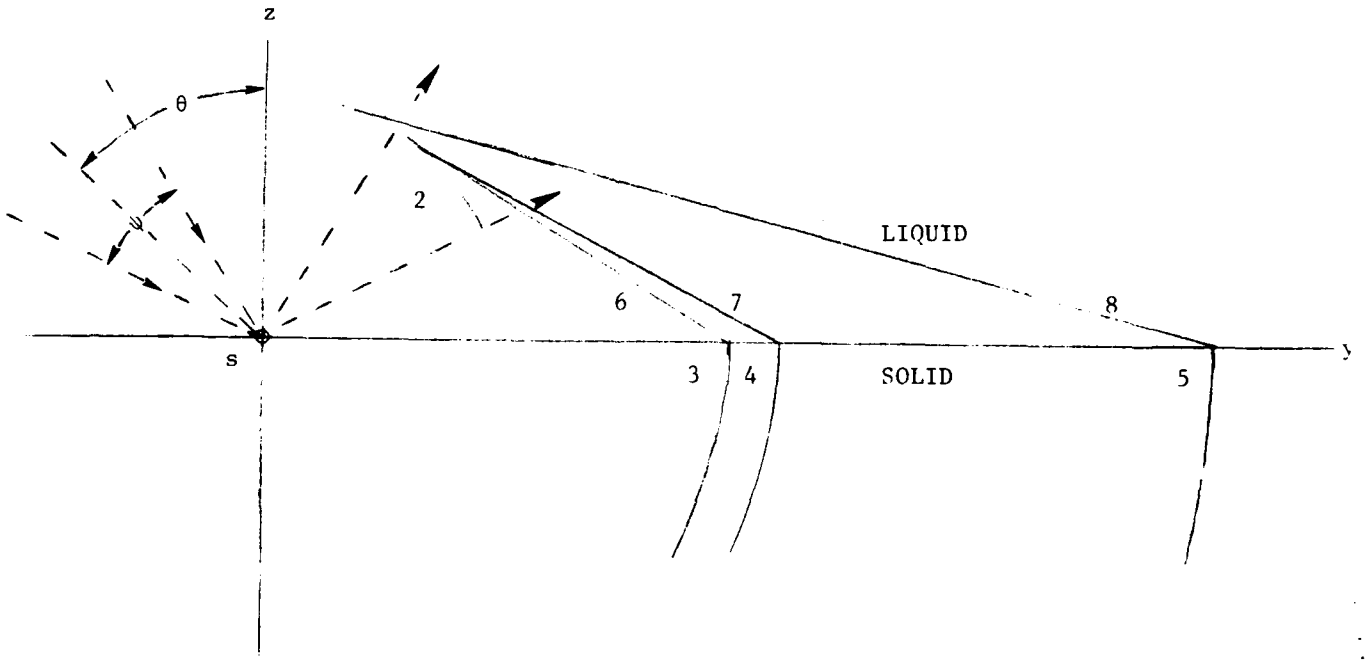

Fig. 3. Side view of wave fronts generated by a spherical source focused at the surface of the solid.

We now have one less wave in the liquid, namely the propagated wave. If the incident cone, Ψ, includes all three critical angles, θ_L, θ_S, θ_R, the remaining waves will be present in the liquid. Our experimental procedure utilizes a point receiver in the center of the reflected cone. Therefore, if we scan the source and receiver beginning at a small angle of incidence, the waves intercepted by the receiver will be a function of the angles as follows. Table 1 represents the cases where $\Psi > \theta_S - \theta_L$ and $\theta_R - \theta_S < \Psi < \theta_S - \theta_L$.

TABLE 1

$\Psi > \theta_S - \theta_L$		$\theta_R - \theta_S < \Psi < \theta_S - \theta_L$	
θ	Wave	θ	Wave
>0 , $< \theta_L - \Psi/2$	2	>0 , $< \theta_L - \Psi/2$	2
$\geq\theta_L - \Psi/2$, $< \theta_S - \Psi/2$	2,8	$\geq\theta_L - \Psi/2$, $< \theta_L + \Psi/2$	2,8
$\geq\theta_S - \Psi/2$, $< \theta_R - \Psi/2$	2,7,8	$\geq\theta_L + \Psi/2$, $< \theta_S - \Psi/2$	2
$\geq\theta_R - \Psi/2$, $< \theta_L + \Psi/2$	2,6,7,8	$\geq\theta_S - \Psi/2$, $< \theta_R - \Psi/2$	2,7
$\geq\theta_L + \Psi/2$, $< \theta_S + \Psi/2$	2,6,7	$\geq\theta_R - \Psi/2$, $< \theta_S + \Psi/2$	2,6,7
$\geq\theta_S + \Psi/2$, $< \theta_R + \Psi/2$	2,6	$\geq\theta_S + \Psi/2$, $< \theta_R + \Psi/2$	2,6
$\geq\theta_R + \Psi/2$	2	$\geq\theta_R + \Psi/2$	2

This is to be compared with the case of plane wave illumination ($\Psi = 0$) shown in Table 2. Note, that in this case each wave is interrogated in sequence.

It appears, then, that in attempting to simplify the system for imaging reasons we may have complicated the signal interpretation process. On the other hand, as evidenced by the experiments described elsewhere in this report, these complications may not be significant.

TABLE 2

$\Psi = 0$	
θ	Wave
> 0 , $< \theta_L$	2
$= \theta_L$	2,8
$> \theta_L$, $< \theta_S$	2
$= \theta_S$	2,7
$> \theta_S$ $< \theta_R$	2
$= \theta_R$	2,6
$> \theta_R$	2

2.2 Plane of Solid

In the preceding discussion, we have examined the system in the y-z plane. The transmitted cone has extent in the other directions as well. Returning to Fig. 1, we see that surface waves are generated over a wedge of angles emanating from the focal point on the surface. This wedge of surface waves reradiates a head wave back into the water, and therefore, must make a contribution to the detected signal.

The wedge of surface waves predicted by geometric theory, as shown in Fig. 4, will subtend an angle Ψ' which depends on the angle of incidence of the lens axis θ, and the angle subtended by the lens aperture from the lens focus Ψ.

$$\Psi' \simeq 2\tan^{-1}\left[\frac{\tan(\Psi/2)}{\sin\theta}\right] \qquad (1)$$

Thus, the wedge of surface waves always has an opening angle Ψ' which is somewhat larger than the opening angle of the lens Ψ.

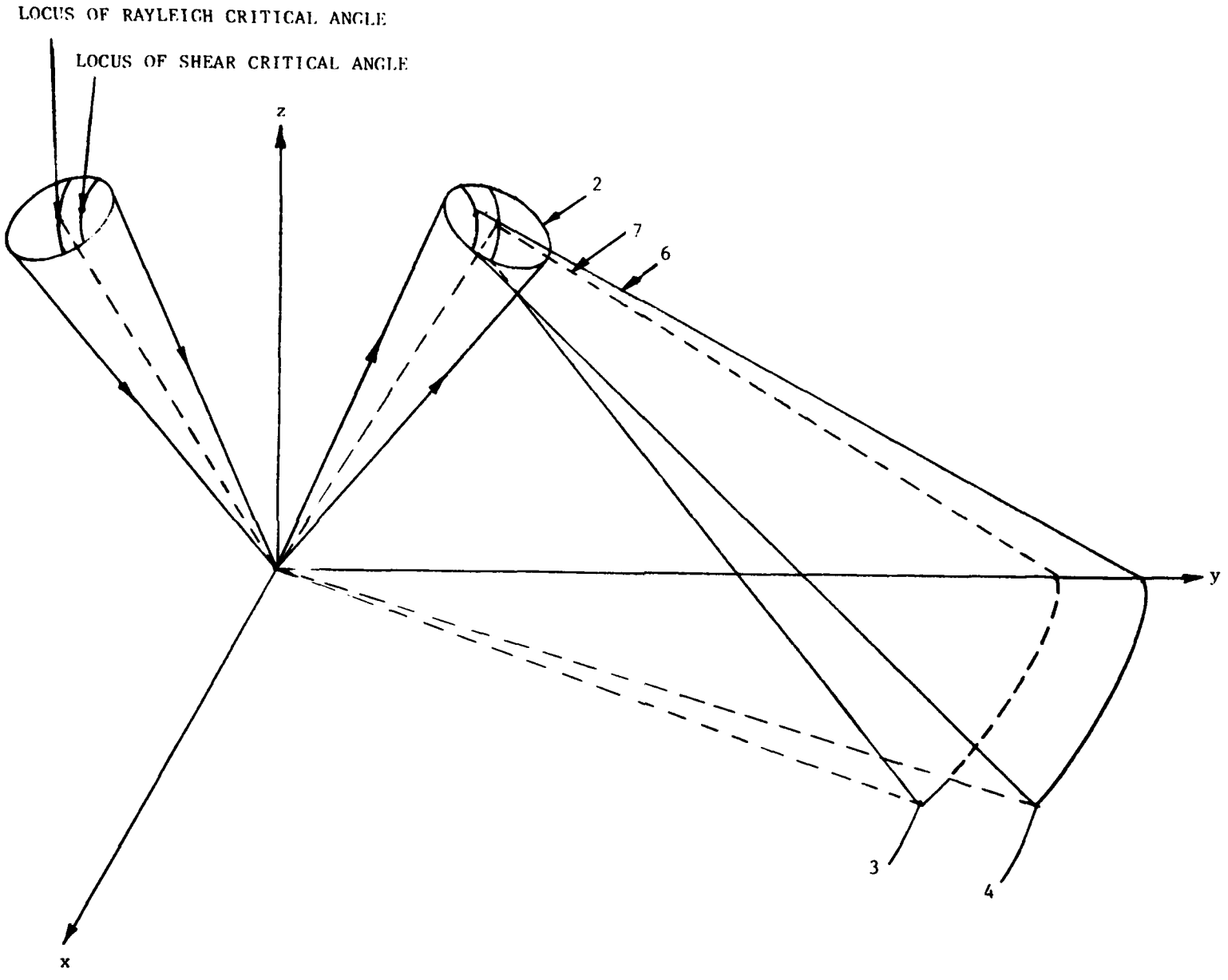

Fig. 4. Isometric sketch of the wave fronts generated by a spherical source focused at the surface of a solid.

From the foregoing, it is clear that we cannot avoid contributions at the detector from waves reradiated by the wedge of surface waves. However, it is not evident that this will lead to results differing significantly from those expected for incident plane waves.

From a geometrical standpoint, we note that a wedge of surface waves will produce a conically shaped diverging wave front, as shown in Fig. 4, of reradiated waves which impinge on the point detector. These conical surfaces will be characterized by a cone with opening angle Ψ and an axis parallel to the axis of the lens in the plane of incidence.

The specularly reflected incident rays will produce a diverging spherical wavefront which also impinges on the same detector. The phase difference between the conical (nonspecular reflected) and spherical (specularly reflected) wavefronts in the plane of incidence should be the same as the phase difference between an incident specularly reflected plane wave and its nonspecularly reflected counterpart which is also plane. Away from the plane of incidence, of course, this statement no longer holds. Thus, if a very small point detector is used, the effect of off-axis rays should be greatly reduced if not eliminated entirely.

For example, in experiments on quartz and copper, we obtain results that are very similar to those of other workers who assumed incident plane wave fronts. Thus, we conclude that even for anisotropic materials (which will distort the reradiated conical wavefronts) off-axis excitation will probably not have a major effect on measurements. Theoretical calculations and further experiments in progress will clarify these points at a later date.

2.3 Focused Beams

The preceding sections dealt with the various waves generated on a surface by a point source. In fact, a focused transducer does not focus to a point since this would necessarily imply infinite intensity. A good review of the behavior of sound in the vicinity of a focus is given by Rozenberg.[3] We will select the pertinent results without showing the analysis since this is readily available in Rozenberg and other references.

For a spherical radiator of half angle, α_m, radius, F, and uniform pressure amplitude at the surface, p_o, the pressure at the point ρ, z is

$$p(\rho,z) = kFp_o\int_o^{\alpha_m} \exp(ikz\cos\alpha)J_o(k\rho\sin\alpha)\sin\alpha d\alpha \qquad (2)$$

where ρ,z are cylindrical coordinates with origin at the center of curvature,

$k = 2\pi/\lambda$,

λ = wavelength,

α = angular coordinate,

J_o = Bessel function of zero order.

In the center of the focal spot, $\rho = z = 0$, the pressure attains the maximum

$$p_F = kFp_o(1 - \cos\alpha_m). \qquad (3)$$

The pressure gain is, therefore,

$$G_p = p_F/p_o = kF(1 - \cos\alpha_m). \qquad (4)$$

The transducer used in our experiment has the parameters F = 10 cm, $\alpha_m = 7°$, f $\simeq$ 4 MHz yielding a pressure gain $G_p = 12.5$.

The pressure distribution in the focal plane is

$$p(\rho) = p_F\,\frac{2J_1(k\rho\alpha_m)}{k\rho\alpha_m}\,, \qquad (5)$$

where J_1 = Bessel function of first order.

The radius of the Airy circle (where J_1 attains its first zero) is

$$\rho_o = 0.61 \frac{\lambda}{\alpha_m} \simeq 0.61 \frac{\lambda F}{R} , \tag{6}$$

where R = radius of the transducer.

The pressure distribution along the z-axis is more complicated, showing the result that the pressure maximum does not always lie in the focal plane. Also, unlike optics, the distribution is not symmetric about the focal point. Tartakovskii derived the expression shown below.[4]

$$\frac{p(z)}{p_F} = \frac{\sin[kz/2(1 - \cos \alpha_m)]}{kz/2(1 - \cos \alpha_m)(1 + z/F)} . \tag{7}$$

The relative displacement of the pressure maximum from the focus is approximated by

$$\frac{z_F}{F} = \frac{1}{1 - G_p^2/12} \simeq \frac{12}{G_p^2} . \tag{8}$$

For our case, $z_F/F \simeq - 0.0768$. That is, the pressure maximum is 0.768 cm closer to the transducer than is the focal plane.

The velocity gain at the focus becomes

$$G_v = kF \frac{\sin^2 \alpha_m}{2} = G_p \cos^2(\alpha_m/2) \tag{9}$$

For small angles, α_m, such as in our case, $G_v \simeq G_p$. The intensity gain G_I, defined as

$$G_I = \frac{I_F}{I_o} = \frac{p_F v_F}{p_o v_o} = G_p G_v . \tag{10}$$

In our case, with $G_v \simeq G_p = 12$, the resulting gain is $G_I = 144$. Thus, even modest intensities at the transducer face can result in large values at the focus.

The shape of the wave front as a function of z, when considered by geometrical acoustics, is a converging sphere which collapses to a point at focus followed by a diverging sphere. When diffraction is considered, the converging spherical wave front changes to a plane

near the focus and then diverges again. Born and Wolf present a particularly detailed analysis of light waves in the vicinity of the focus.[5] Their results show that in the immediate neighborhood of the focus the wave front is substantially plane with cophasal surfaces spaced by $\lambda(1 - R^2/4F^2)$ rather than λ. At the first zero of the Airy pattern, the phase fronts shift by π radians leading on the converging side and lagging on the diverging side of the focus. In our case, the cophasal surfaces will be separated by 0.9961λ which could be interpreted as a frequency shift of 0.39%. The following figures from Born and Wolf are reproduced to show the kind of detailed behavior experienced by the wave front near the focus. Note that a phase anomaly of $\pi/2$ occurs at the focus. This is illustrated more clearly by the following figure, also from Born and Wolf.

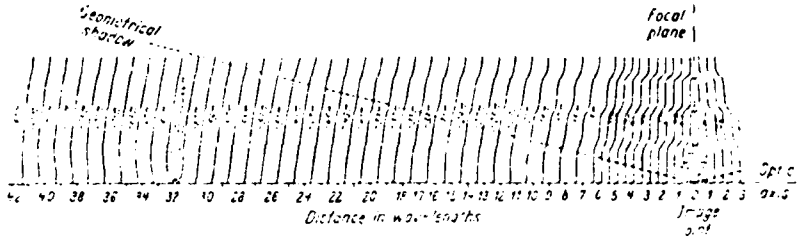

Fig. 8.45. Profiles of the co-phasal surfaces $\phi(u, v) =$ constant near the geometrical focus, calculated with $\lambda = 5 \cdot 10^{-5}$ cm, $a = 2{\cdot}5$ cm, $f = 10$ cm.
(After G. W. FARNELL, *Canad. J. Phys.*, **35** (1957), 780.)†

Fig. 5. Profiles of the wave fronts in the vicinity of focus.

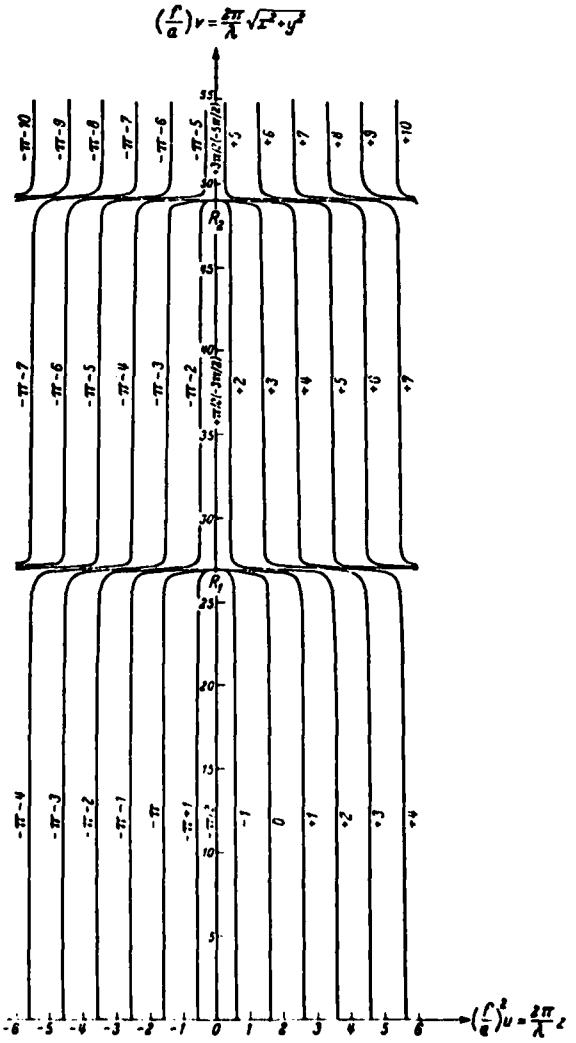

Fig. 8.46. Profiles of co-phasal surfaces in the immediate neighbourhood of the geometrical focal plane of an $f/3.5$ homocentric pencil. OR_1 and OR_2 are the radii of the first and second Airy dark rings.

(After E. H. Linfoot and E. Wolf, *Proc. Phys. Soc.*, B, **69** (1956), 827.)

Fig. 6. Detail of wave fronts in the vicinity of the focus.

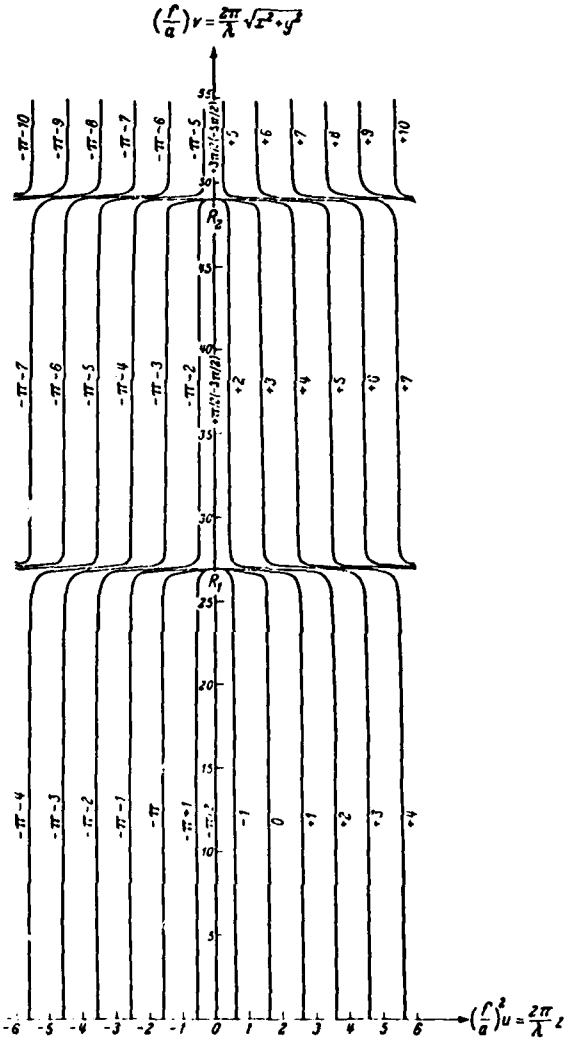

Fig. 8.46. Profiles of co-phasal surfaces in the immediate neighbourhood of the geometrical focal plane of an *f*/3.5 homocentric pencil. OR_1 and OR_2 are the radii of the first and second Airy dark rings.

(After E. H. Linfoot and E. Wolf, *Proc. Phys. Soc.*, B, **69** (1956), 827.)

Fig. 6. Detail of wave fronts in the vicinity of the focus.

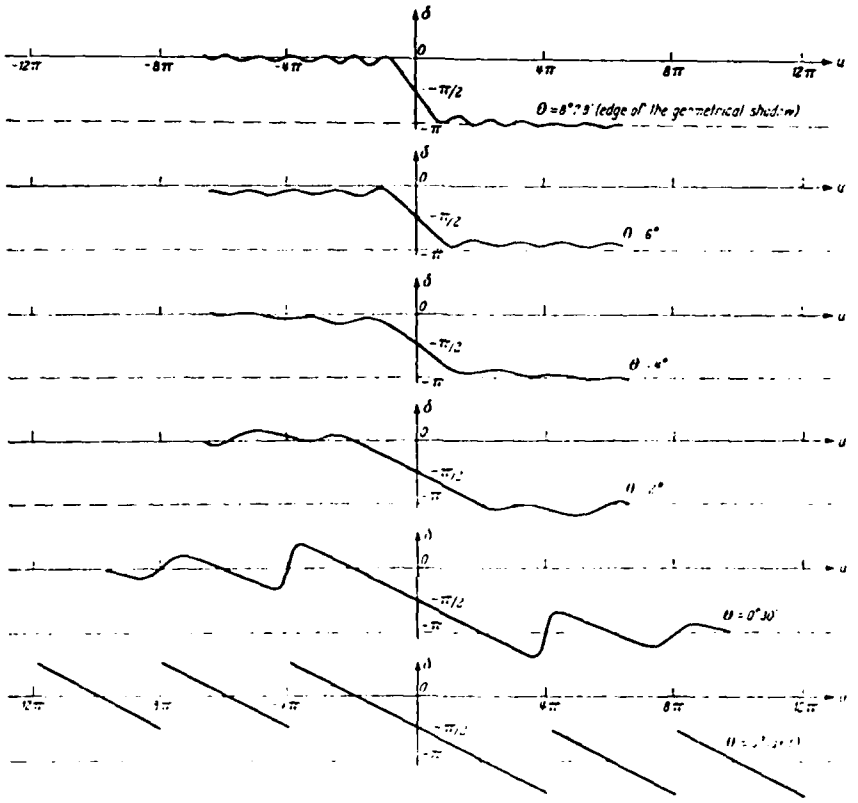

Fig. 8.47. Phase anomaly δ along geometrical rays through the focus of a homocentric $f/3.5$ pencil. The angle θ denotes the inclination of the ray to the axis. (After E. H. Linfoot and E. Wolf, *Proc. Phys. Soc.*, B, **69** (1956), 827.)

Fig. 7. Details of the phase of the light wave along rays passing through the focus.

What we have, then, is an elliptical spot on the surface that is generating surface waves when one or more critical angles are present in the incident cone. The smallest diameter of the ellipse as given by Eq. (6) will be $D = 4.88\ \lambda_w$, where λ_w = wavelength in water. The surface wavelengths are, generally speaking, longer than

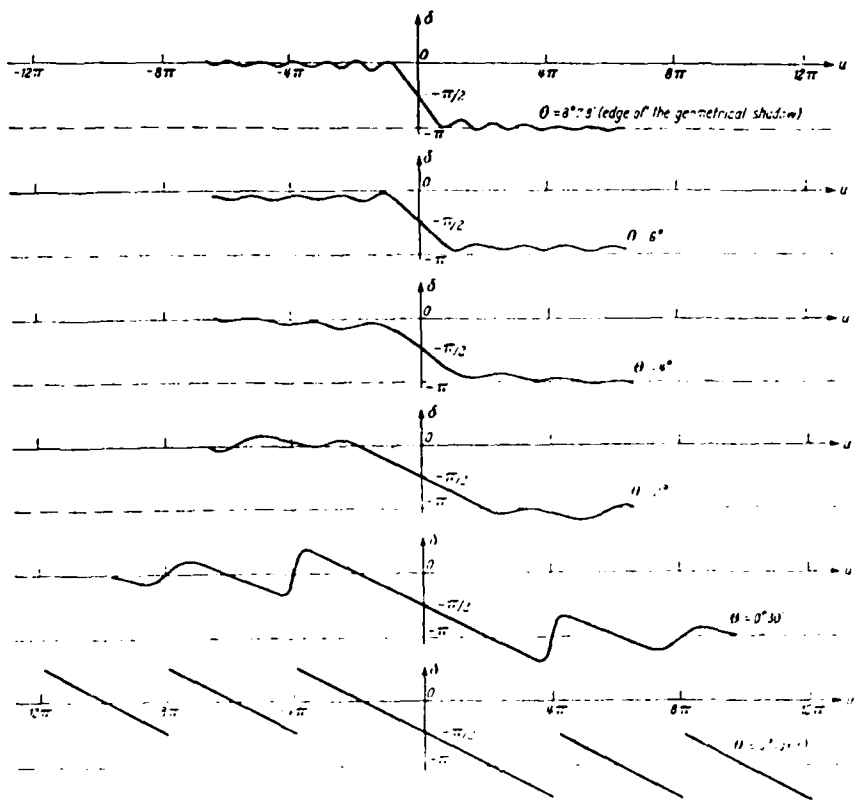

Fig. 8.47. Phase anomaly δ along geometrical rays through the focus of a homocentric $f/3.5$ pencil. The angle θ denotes the inclination of the ray to the axis. (After E. H. LINFOOT and E. WOLF, *Proc. Phys. Soc.*, B, **69** (1956), 827.)

Fig. 7. Details of the phase of the light wave along rays passing through the focus.

What we have, then, is an elliptical spot on the surface that is generating surface waves when one or more critical angles are present in the incident cone. The smallest diameter of the ellipse as given by Eq. (6) will be $D = 4.88\ \lambda_w$, where λ_w = wavelength in water. The surface wavelengths are, generally speaking, longer than

λ_w. Taking copper as a specific example; $\lambda_L = 3.1\ \lambda_w$, $\lambda_S = 1.4\ \lambda_w$, and $\lambda_R = 1.3\ \lambda_w$. Hence, the source aperture size in terms of wavelengths becomes $D = 1.6\ \lambda_L = 3.5\ \lambda_S = 3.7\ \lambda_R$. These are very small apertures which will have wide radiation patterns. For the uniformly weighted aperture, the corresponding angular extent of the wedge of surface waves will be $\Psi_L = 77°$, $\Psi_S = 33°$, $\Psi_R = 31°$. These values are, of course, not precisely correct because of the assumption of a uniform driving function. In fact, it will more nearly approximate a Gaussian distribution.

It is obvious that the propagation velocities in the material will have an important effect on the spread of the surface waves. Copper happens to propagate sound fairly slowly. Aluminum, having higher propagation velocity, will show a corresponding greater spread of surface waves from the focal point. Beryllium, on the other hand, would produce a narrower spread.

2.4 Nonlinearity

Since it is reasonable to suppose that the intensity level near focus is high enough to couple energy into nonlinear terms, we discuss this aspect of focused beams further. We again rely on extremely well written accounts by Rozenberg and by Naugol'nykl, and quote only pertinent results.[6] It is well known that the propagation of compressional waves must be a nonlinear process.[7] This is so because the velocity of propagation is a function of density, and compressional waves result in density fluctuations. Thus, in the compression half cycle, the velocity increases while it decreases in the rarefaction half cycle. Thus, a sinusoidal wave grows into a sawtooth after propagating sufficiently far.

In our experimental system, we would expect nonlinearity in the water path, as was shown in the last quarterly report.[8] The question is what happens at the boundary. Does the material also respond nonlinearly or not? Breazeale has reported nonlinear behavior

in solids when driven with finite amplitude compressional waves.[9] Preliminary data reported in our last quarterly showed only that the harmonic content of the wave seemed to change upon reflection from the surface. This could be due to differential phase shifting of the harmonics, or by the nonlinear response of the reflector.

Consider a spherical wave of half angle α_m and radius F propagating to the surface of a sphere of radius r_f as shown in Fig. 8.

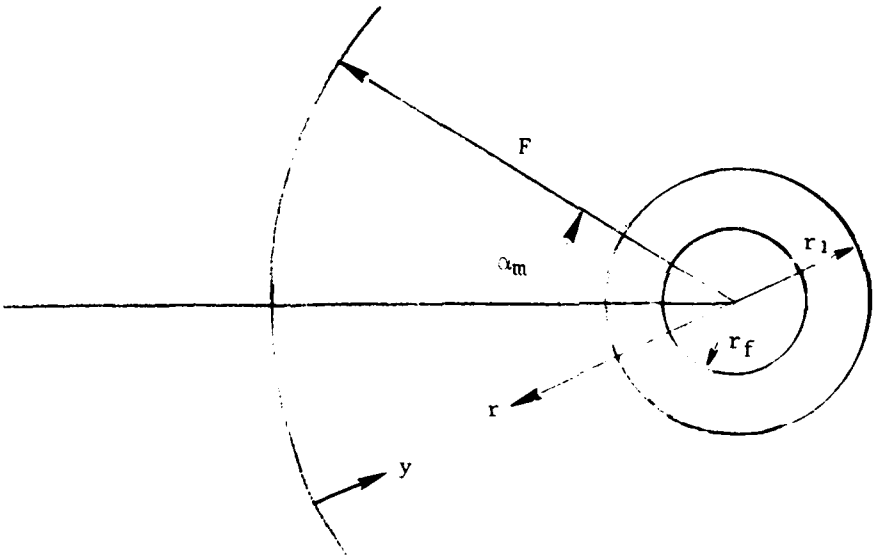

Fig. 8. Waves propagating from a point source.

We assume that in the region $r_1 < r < F$, the wave propagates with little attenuation, but does distort due to nonlinear behavior. At $r = r_1$, the previously sinusoidal wave transforms to a sawtooth. We assume that from this point on the wave is attenuated by a large attenuation.

Up to this point in the argument, we have used geometric theory. We know, however, that diffraction must play a role. We define the distance $r = r_f$ as that distance where the wave reaches the particle velocity at the focus, $r = 0$, predicted by diffraction theory. Analyses carried out by Rozenberg, Naugol'nykh, and Sutin[10] have shown that, for small nonlinearities, the gain is increased and the focal region is narrowed.

Returning to the analysis, we assume that the particle velocity

$$v = v_o F/r \quad \text{for} \quad r_f < r < F$$

$$= v_f = v_o k F^2 \frac{\sin^2 \alpha_m}{2} \quad \text{for} \quad r \leq r_f. \tag{11}$$

In reference 6, it is shown that the actual particle velocity amplitude at the center of the focal spot can be approximated by

$$\bar{v}_f = \frac{v_o G_v}{m + \frac{\varepsilon v_o}{\pi c} kFG_v} \tag{12}$$

where $m = 1 - 1/\pi$,

and $\varepsilon = \frac{1}{2} \frac{\partial c^2}{\partial \rho^2} \frac{\rho_o}{c} + 1.$

It is evident from this equation that v_f reaches a limit with respect to v_o. Thus, it becomes inefficient to increase the particle velocity at the transducer since the particle velocity at focus saturates. If energy concentration is the goal, the system may be optimized with respect to F, λ, and α_m.

Sutin analyzes the problem in greater detail to obtain an approximation to wave profiles at and near focus, as well as spectral content. Figure 9, taken from Sutin's paper, shows the wave profiles at three points near focus for a very modest nonlinearity parameter, σ, given by

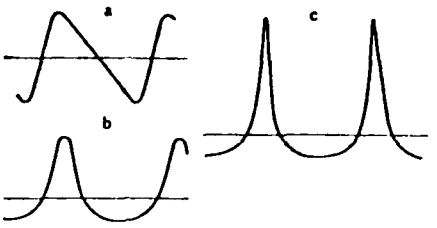

Fig. 9. Wave profile at various points for $\sigma = 0.7$ ($\sigma = 1$ leads to formation of a shock, $\sigma > 3$ leads to a sawtooth): (a) on axis at $r = r_f$, (b) off-axis in the focal plane, and (c) at the focus.

$$\sigma = \sigma_o |\ln F/r| \tag{13}$$

$$\text{where } \sigma_o = \frac{\pi(\gamma + 1)\, p_o\, F}{\rho \lambda c^2}$$

As can be surmised from these profiles, the spectrum of the waveform will change considerably when passing through the focal region.

Van Buren has considered the effect of the reflection of finite amplitude waves by a solid.[11] The conclusion is that the behavior of the reflection coefficient has a profound influence on the reflected wave. For example, he shows that a plane wave of sinusoidal profile, launched into a nonlinear medium, will gradually become distorted through the generation of harmonics. Upon reflection, each harmonic component undergoes the same phase shift changing the relationship between them. This results in a reversed sawtooth profile. Upon further propagation, newly generated harmonics eventually overcome the propagated, phase shifted initial harmonics, to once more make the profile sinusoidal (this is true only for 180° phase shift). If the wave continues past this point, it will again distort.

The waveform reverts to sinusoidal form approximately the same distance from the reflector that it was initially launched from.

Breazeale suggested that since a 180° phase shift occurs at the focus of a converging wave, a similar reaction should occur.[12] That is, if the transducer launches a converging sinusoidal wave into a nonlinear medium (water) and measurements of its harmonics or profile are made along the principle axis, we should expect the second and third harmonics to grow as the focus is approached (profile approaching a sawtooth). After passing through focus and propagating one focal distance, the profile will again be sinusoidal. This is under the assumption that frequency dependent attenuation does not occur. If it does, an analysis such as described by Sutin must be followed. Therefore, in our experiment we can conclude that any appearance of harmonics in our output, beyond those present in the input, must be due to the reflection coefficient of the solid. This does not necessarily imply nonlinear response of the solid since other material parameters may produce phase shifts different than 180°. It remains to be seen just what these might be.

3.0 DYNAMICS OF ELASTIC SOLIDS

3.1 Isotropic Elastic Solids (Linear Approximation)

The simplest case of an elastic solid is that of a homogenous, isotropic, lossless, linear material. By linear, we mean that the full and correct strain tensor ($z,k,\ell = 1,2,3$)

$$U_{ik} = \frac{1}{2}\left(\frac{\partial U_i}{\partial X_k} + \frac{\partial U_k}{\partial X_i} + \frac{\partial U_\ell}{\partial X_i}\ \frac{\partial U_\ell}{\partial X_k}\right) \tag{14}$$

is approximated by dropping the higher order terms $\frac{\partial U_\ell}{\partial X_i}\ \frac{\partial U_\ell}{\partial X_k}$.

It should be noted that this is equivalent to dropping all interactions (and amplitude dependent dispersion, etc.) and, strictly speaking, would mean that neither energy or momentum could be propagated across the material in the form of elastic waves. Propagation ultimately requires interactions (nonlinear response) between the various parts of the solid.

Note, for example, that the energy density ε (adiabatic conditions) is a scalar function of the full strain tensor[13] given by Eq. (14). If the higher order terms are dropped in Eq. (14), we still obtain a more or less accurate estimate of the observed energy (and momentum) densities in the wave (the linear estimate), but strictly speaking, no actual wave would propagate if these nonlinear terms were missing. Hence, the notion that purely linear elastic waves exist is incorrect although this assumption is an excellent approximation when amplitudes are small.

Let us assume, then, that the strain tensor may be approximated by the expression

$$U_{ik} \simeq \frac{1}{2}\left(\frac{\partial U_i}{\partial X_k} + \frac{\partial U_k}{\partial X_i}\right). \tag{15}$$

The equation of motion of any solid[13] in Classical Mechanics (Newton's second law) relates the forces $\partial\sigma_{ik}/\partial X_k$ due to the internal

stresses σ_{ik} to the acceleration $\ddot{U}_i$ and the mass density ρ via

$$\rho\ddot{U}_i = \partial\sigma_{ik}/\partial X_k. \tag{16}$$

After some manipulation[13] (also see 28 September 1981 Quarterly Report), this may be rewritten in vector notation for a linear isotropic solid as

$$\rho\ddot{\overline{U}} = \mu\nabla^2\overline{U} + (\lambda+\mu)\nabla(\nabla\cdot\overline{U}) \tag{17}$$

where μ and λ are the two Lamé coefficients. These coefficients may also be expressed in terms of the Young's modulus E, and Poisson's ratio σ of the isotropic solid via

$$\lambda + \mu = \frac{E}{2(1+\sigma)(1-2\sigma)} \tag{18}$$

$$\mu = \frac{E}{2(1+\sigma)} \ . \tag{19}$$

It is clear that a linear, isotropic elastic solid requires only two elastic constants (E, σ or λ, μ etc.) for its description. Moreover, the particle displacement may always be decomposed into the sum of a dilational part $\nabla\phi$ having nonzero divergence (i.e. nonzero volume change) and a rotational part ($\nabla X\overline{\Psi}$) having no divergence (zero volume change)

$$\overline{U} = \nabla\phi + \nabla X\overline{\Psi} \ .$$

By substituting $\overline{U}$ into the approximate expression (Fq. (17)), it may be shown that the scalar potential ϕ corresponds to a pure mode bulk longitudinal wave and obeys the linear wave equation

$$\nabla^2\phi - \frac{1}{C_L^2}\frac{\partial^2\phi}{\partial t^2} = 0 \tag{20}$$

with propagation velocity C_T in all directions

$$C_L^2 = \frac{(\lambda+2\mu)}{\rho} = \frac{E(1-\sigma)}{\rho(1+\sigma)(1-2\sigma)} \quad . \tag{21}$$

Similarly, the vector potential $\overline{\Psi}$ corresponds to the pure mode bulk shear or transverse wave, and obeys the linear wave equation

$$\nabla^2\overline{\Psi} - \frac{1}{C_T^2} \frac{\partial^2\overline{\Psi}}{\partial t^2} = 0 \tag{22}$$

with propagation velocity C_T in any direction.

$$C_T^2 = \frac{\mu}{\rho} = \frac{E}{2\rho(1+\sigma)} \quad . \tag{23}$$

Again, we remind the reader that these are linear approximations which result because we have neglected higher order strains in in Eq. (14).

3.2 Energy Flux and Snell's Law

The energy flux directions of both the longitudinal and the shear wave in an isotropic medium lie along the wave normals.[14] That is, the slowness surfaces (inverse velocity surfaces) are always circles.[15] Because the slowness surfaces are simple in such materials, Snell's law provides an adequate description of the refraction at a liquid-solid boundary. Such a refraction (liquid to solid) can produce just two bulk waves (longitudinal and transverse). Provided attenuation is small (lossless approximation), the two critical angles θ_L and θ_T will be given by Snell's law as

$$\frac{\sin\theta_L}{V_w} = \frac{\sin\pi/2}{C_L} = \frac{1}{C_L} \tag{24}$$

and

$$\frac{\sin\theta_T}{V_w} = \frac{\sin\pi/2}{C_T} = \frac{1}{C_T} \tag{25}$$

where V_w is the longitudinal wave velocity in water.

Real isotropic materials include glasses, ceramics, powder composites, and any alloy or other polycrystalline material (crystals are assumed to be small compared with typical wavelengths in the solid) that has been prepared without grain alignments, residual stress fields, and the like.

In all such materials, we would expect to see two critical angles; one for the shear (θ_T) and one for the longitudinal wave (θ_L). These angles would be in addition to the "Rayleigh-type" critical angle θ_R which occurs slightly beyond the shear critical angle θ_T.

Given information from the observed critical angles, one could always infer λ and μ. If a density measurement ρ is made, we would then have a complete linear description of the isotropic elastic material. That is, the second order elastic constants of the isotropic solid (C_{ij}) could be calculated[13,14] from

$$C_{11} = C_{22} = C_{22} = (\lambda+2\mu)$$

$$C_{12} = C_{21} = C_{13} = C_{31} = C_{23} = C_{32} = \lambda \qquad (26)$$

$$C_{44} = C_{55} = C_{66} = \mu$$

3.3 Anisotropic Materials (Linear Approximation)

In isotropic solids the frequency ω is always proportional to the wave number $k = |\bar{k}|$. That is,

$$\omega = C_L k$$

and $$\omega = C_T K \qquad (27)$$

In anisotropic materials this is no longer a valid statement. The general equation of motion as before is

$$\rho \ddot{U}_i = \partial \sigma_{ik} / \partial X_k \ , \qquad (28)$$

but the stress tensor σ_{ik} is now a more complex general tensor of the form

$$\sigma_{ik} = \lambda_{ik\ell m}\, U_{\ell m} \tag{29}$$

where the symmetric tensor $\lambda_{ik\ell m}$ describes the adiabatic moduli of elasticity and $U_{\ell m}$ is the strain tensor (linear approximation of Eq. (15)). Substituting this into the equation of motion and noting the symmetry of $\lambda_{ik\ell m}$, one has

$$\rho \ddot{U}_i \simeq \lambda_{ik\ell m} \frac{\partial^2 U_m}{\partial X_k \, \partial X_\ell} \,. \tag{30}$$

Consider a monochromatic elastic wave (the linear approximation makes this possible) in such a solid. Then

$$U_i = U_{oi}\, e^{i(\bar{k}\cdot\bar{r}-\omega t)} \tag{31}$$

where $\bar{k}$ is a function of ω which satisifes Eq. (30) and is clearly no longer as simple as Eq. (27) for isotropic materials. Substitution of U_i (or U_m, etc.) into Eq. (30) gives[13]

$$(\rho\omega^2 \delta_{im} - \lambda_{ik\ell m}\, k_k\, k_\ell)\, U_m = 0. \tag{32}$$

This equation is actually three homogeneous equations in the unknown particle displacements $U_1 = U_x$, $U_2 = U_y$ and $U_3 = U_z$. nontrivial solution requires that the determinant of the coefficients vanish, namely

$$|\lambda_{ik\ell m}\, k_k\, k_\ell - \rho\omega^2 \delta_{im}| = 0. \tag{33}$$

This is a cubic equation in ω^2. Each of the three roots of this equation provides a different functional relation between the frequency and wave number k (unless the material is isotropic).

Now the direction of the energy flux is given by the group velocity $\partial\omega/\partial\bar{k}$. In isotropic materials ω is proportional to the magnitude of $\bar{k}$, and therefore, does not depend on its direction. Hence, the energy flux in isotropic materials must lie along the direction of the wave vectors (or wave normals) for both longitudinal and shear waves.

In the case of anisotropic materials, the situation is quite different. In that case, the direction of propagation of the energy flux is along the direction of the group velocity $\partial\omega/\partial\bar{k}$ and not along $\bar{k}$. Now, since there are three functional relations between ω and $\bar{k}$, there are, in general, three different velocities of propagation in any anisotropic material.[13-15]

3.4 Modifications of Snell's Law

Owing to the fact that the energy flux directions and the wave vectors are not generally colinear in anisotropic materials, the interpretation of critical angles becomes more difficult. Hennecke[2] has shown that the critical angles θ_c for quasilongitudinal and quasishear waves should be given by the expression (I = incident, R = refracted)

$$\sin\theta_c = \frac{V_{Ic}}{V_{Rc}} \frac{\cos\psi_c}{\cos\beta_c} \tag{34}$$

where V_{Rc} is the velocity of a wave which has its energy flux vector parallel to the liquid-solid interface. It is not the velocity of a body wave propagating in a direction parallel to the interface.

Following Hennecke[2], we may derive this expression by writing the scalar product of the group velocity $\bar{g}$ of the refracted wave (this is in the same direction as the energy flux) and a vector $\bar{b}$. The vector $\bar{b}$ is the vector sum of all the slowness vectors satisfying the reflection-refraction problem at the interface. Now, $\bar{b}$ can be written in terms of the refracted wave as $\bar{M}_R - Z_R\bar{\nu}$ where $\bar{M}_R$

is the slowness vector of the refracted wave ($\bar{M}_R = \bar{N}_R/V_R$; $\bar{N}_R$ is the wave normal of the refracted wave, V_R is the magnitude of the refracted wave velocity), ν is the normal to the liquid-solid interface and Z_R is a number characterizing the refracted wave. Therefore,

$$\bar{b}\cdot\bar{g} = \bar{M}_R\cdot\bar{g} - Z_R\,\bar{\nu}\cdot\bar{g} = \frac{\bar{N}_R}{V_R}\cdot\bar{g} - Z_R\bar{\nu}\cdot\bar{g} \ . \tag{35}$$

Since

$$\bar{g}\cdot\bar{N}_R = V_R,$$

$$\bar{b}\cdot\bar{g} = 1 - Z_R\bar{\nu}\cdot\bar{g} \ . \tag{36}$$

When the critical angle occurs, the energy flux vector and $\bar{g}$ lie parallel to the liquid-solid interface. Therefore, $\bar{g}$ is perpendicular to $\bar{\nu}$ and

$$\bar{b}_c\cdot\bar{g}_c = 1.$$

Since the magnitude of the slowness vector $\bar{b}$ may be determined by the incident angle θ_c from

$$|\bar{b}_c| = \sin\theta_c/V_{Ic}$$

where V_{Ic} is the longitudinal velocity in the liquid (water in this case), we have

$$\bar{b}_c\cdot\bar{g}_c = |\bar{b}_c||\bar{g}_c|\cos\beta_c = \frac{\sin\theta_c}{V_{Ic}}\,|\bar{g}_c|\cos\beta_c = 1 \tag{38}$$

where β_c is the angle between $\bar{b}_c$ and $\bar{g}_c$.

But, we also know that

$$\bar{g}\cdot\bar{M}_R = 1 = \frac{g\cos\psi}{V_R}$$

where ψ is the angle between the normal to the refracted wave and its associated energy flux. At criticality,

$$\bar{g}_c \cdot \bar{M}_{Rc} = \frac{|\bar{g}_c| \cos \psi_c}{V_{Rc}} = 1. \tag{39}$$

Combining Eqs. (38) and (39), we finally have Eq. (34) which is clearly very different from Snell's law. Thus, we see that Snell's law is generally not valid at a liquid-solid interace when the solid is anisotropic.

As Hennecke points out, ψ is not the angle between the slowness vector of the refracted wave $\bar{M}_R$ and the interface, so that a measurement of the critical angle θ_c will not in general be sufficient to determine the refracted velocity V_{Rc}. Hence, the elastic constants cannot be found from such measurements in general. Note also that the angles θ_c and β_c depend in a complex fashion on these same unknown elastic constants via the slowness surfaces of the solid.

The situation is perhaps not as hopeless as Hennecke indicates since one can certainly hope to fit observed critical angle data (as a function of rotation about various symmetry axes) to a model where elastic constants are chosen and varied to fit the data. Moreover, along the pure mode directions of an anisotropic material, Snell's law remains valid (for many of the refracted rays) so that critical angle data along these directions can be related directly to elastic constants.

An interesting conclusion of Hennecke is that there are in fact five critical angles in a material like quartz. We will give experimental evidence of at least two of the five angles he predicts. Such multiple angles are qualitatively similar to the "multiple dips" we reported earlier on several uncontrolled materials. We will see that such multiple dips are almost certainly the response of anisotropic solids.

4.0 EXPERIMENTS

In this report we discuss experiments performed on three representative controlled materials. The three materials are optical glass, a copper single crystal, and a z-cut slab of crystalline quartz. In addition, we are in the process of examining other crystals; the characteristics of which are listed in Table III (see also Fig. 10(a) and 10(b)).

TABLE III Experimental Materials (Crystals)

Name	Crystal System	Description	Orientation
Silicon (Si)	Cubic	Disk: 3.2 cm dia, .9 cm thick	
Quartz (SiO_2)	Hexagonal	Disk: 2.5 cm dia, 1.3 cm thick	(x,y,z cuts)
Lithium Niobate ($LiNbO_3$)	Hexagonal	Disk: 3 cm dia, .75 cm thick	
Spinel ($MgAl_2O_4$)	Cubic	Rod: 2.8 cm dia, 2.5 cm long	
Sapphire (Al_2O_3)	Hexagonal	Disk: 5 cm dia, .35 cm thick	
Copper (Cu)	Cubic	Rod: 2.5 cm dia, 1.9 cm long	(100)
Aluminum (Al)	Cubic	Rod: 2.54 cm dia 2.54 cm long	(100)
Lead (Pb)	Cubic	Rod: 2.54 cm dia, 2.8 cm long	(100)
Silver (Ag)	Cubic	Disk: 1.5 cm dia, .6 cm thick	
Iron (Fe)	Cubic	Rod: 1.0 cm dia, 2.5 cm long	(110)

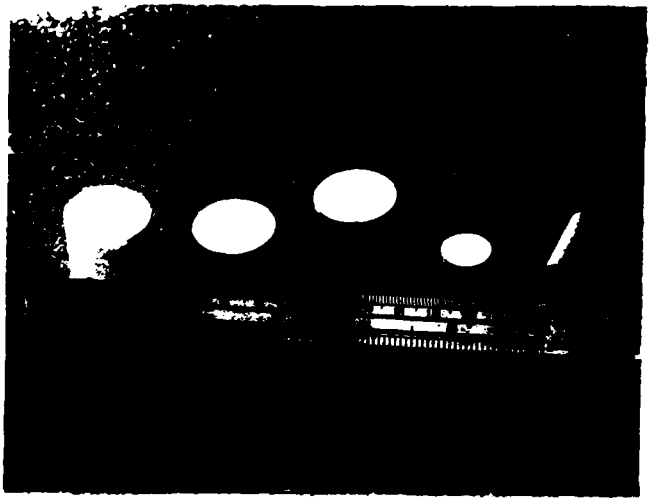

(a) Metal Single Crystals

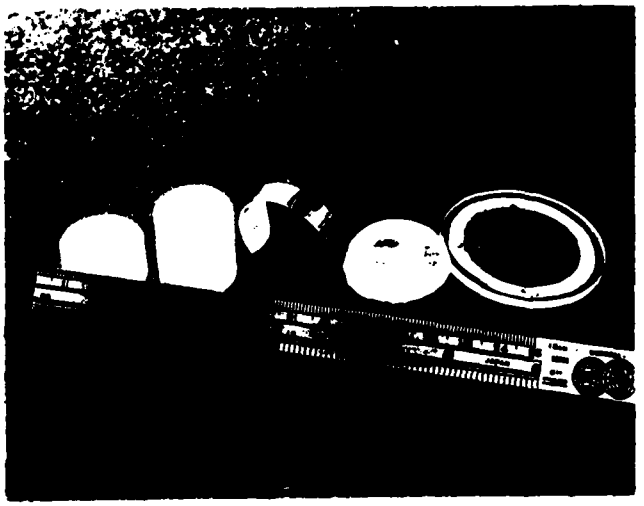

(b) Nonconducting or Semiconducting Crystals

Fig. 10. Single Crystals. (a) We illustrate five metal single crystals identified from left to right as Aℓ, Cu, Pb, Ag, and Fe. All, except the Ag, have a known orientation. (b) From left to right are z-cut quartz, spinel, silicon, lithium niobate, and sapphire. Of these, only the z-cut quartz has a known orientation.

4.1 Optical Glass

One polished surface of a cube of optical glass (L = 2.54 cm) was rotated about an axis (the azimuthal axis of the goniometer) normal to this surface (see Fig. 11), and critical angle measurements made. Figure 12 illustrates an azimuthal plot of the critical angle $\rho = \theta_c$ vs the angle of rotation ϕ about the surface normal. From this figure it is clear that a single Rayleigh-type critical angle $\theta_R \simeq 28.4°$ exists for such an isotropic material.

Since we cannot measure angles less than 15°, the expected amplitude "bump" at the longitudinal critical angle $\theta_L \simeq 11°$ ($\sin \theta_L \simeq 1/2 \sin \theta_S$) on the amplitude curve $R(\theta)$ vs θ has not been observed. However, we know that the shear critical angle θ_S should also produce a small amplitude "bump" before ($\theta_S < \theta_R$) $R(\theta)$ approaches a minimum at θ_R. From the curve of Fig. 13(a), we estimate $\theta_S \simeq 22.5$ which is roughly 6° less than θ_R.

In Fig. 13(a) and (b) we illustrate two sets of measurements of amplitude $R(\theta)$ and phase $\phi(\theta)$ vs the angle of incidence θ taken at two different azimuthal angles ϕ. Note that one of the phase curves (Fig. 13(a)) shows a 360° phase shift (a so-called normal phase curve), whereas the other (Fig. 13(b)) shows "anomalous" character. In fact, four of the phase measurements $\phi(\theta)$ vs θ made at eleven different azimuthal angles ϕ show these same anomalies.

It is clear from these observations that such phase anomalies are not to be attributed to the anisotropic character of a specimen since this glass specimen is clearly isotropic (see Fig. 12). It will happen, however, that anisotropies can influence this phase anomaly as we shall see when we examine crystalline quartz.

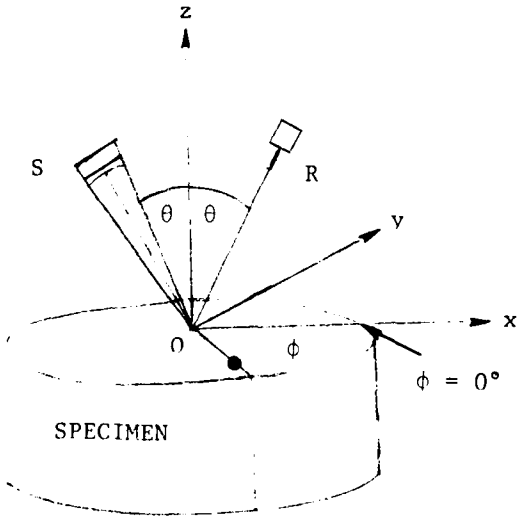

Fig. 11. Rotation of Samples. Samples are arbitrarily marked with a spot as shown. The spot is located along the positive x-axis which initially lies in the incident plane (S-O-R) of the source and receiver. The normal to the specimen surface lies along the z-axis for all azimuthal angles ϕ. We arbitrarily label the x direction $\phi = 0°$ and turn the specimen counterclockwise.

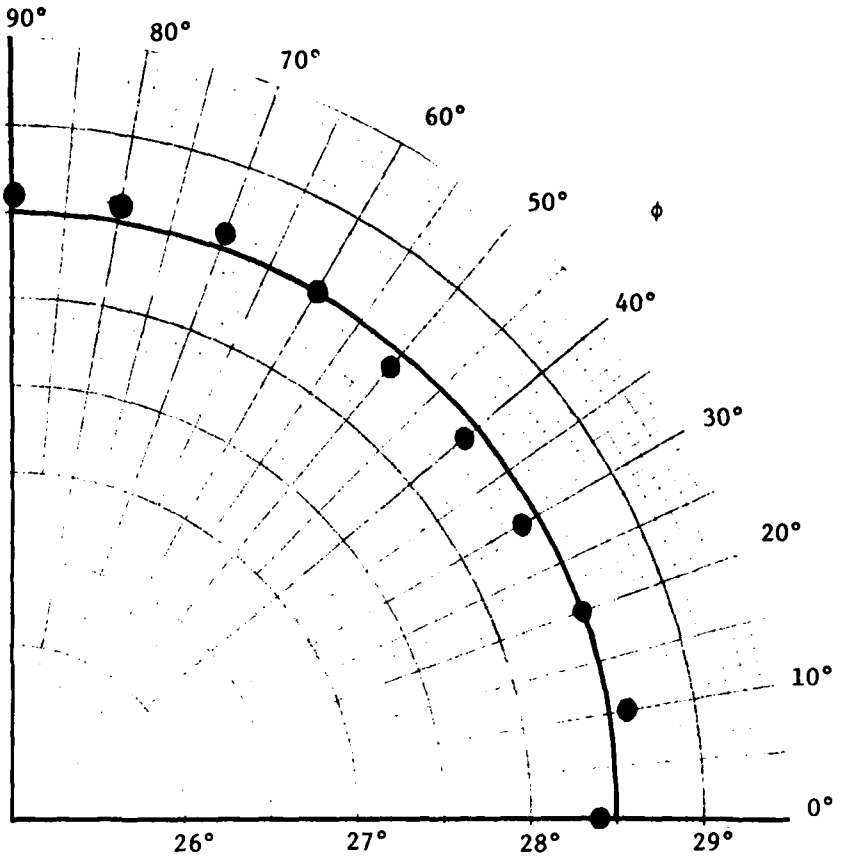

Fig. 12. Critical angle for glass. The figure shows the critical angle as a function of the azimuthal angle ϕ (angle of rotation of the specimen).

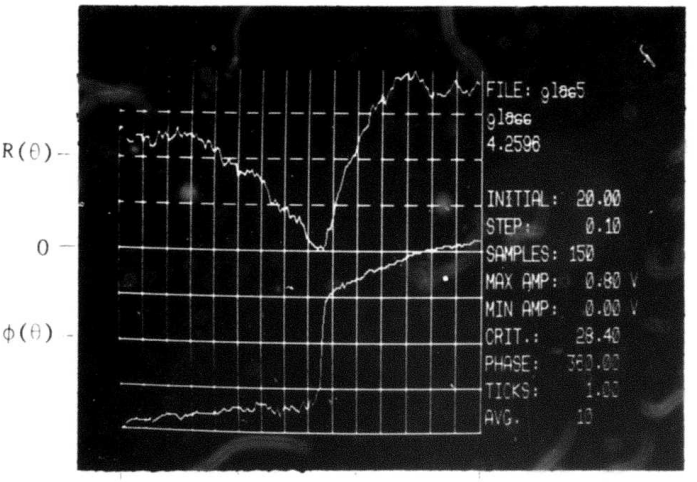

(a) "Normal" Phase Curve $\phi(\theta)$

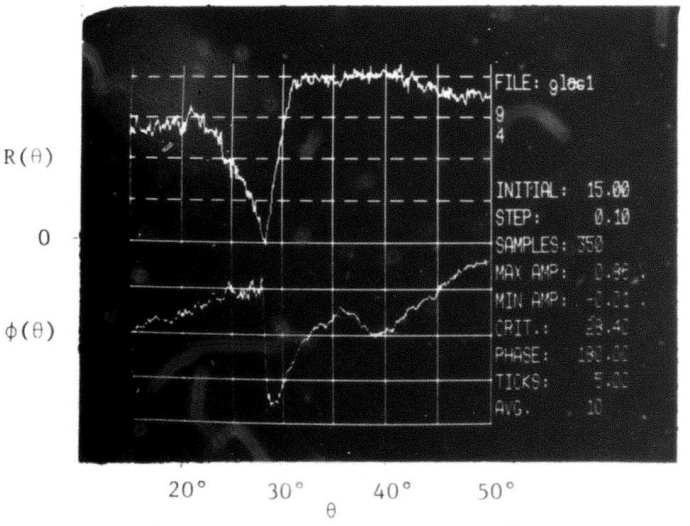

(b) "Anomalous" Phase Curve $\phi(\theta)$

Fig. 13. Amplitude $R(\theta)$ and phase $\phi(\theta)$ measurements vs angle of incidence θ for optical glass. The frequency was 4.3 MHz and the observed critical angle is $\theta_c = 28.4°$. Both normal and anomalous phase curves occur in an isotropic glass specimen.

4.2 Observations On Z-Cut Quartz

As mentioned previously, we have obtained x,y, and z-cut specimens of quartz (see Fig. 14). The experiment reported here was performed on a z-cut plate 1 cm thick by 2.54 cm diameter. Since the z-axis is the symmetry axis, and since quartz is hexagonal, any measured elastic properties (such as, velocity or critical angles, etc.) will necessarily exhibit a 60° angular periodicity for azimuthal angles ϕ about this z-axis.

In Fig. 15 we illustrate a graph of the observed "Rayleigh-type" critical angles θ_c vs the aximuthal angle ϕ defining the plane of incidence of a focused longitudinal wave in water. The term "Rayleigh-type" critical angle used here refers to the fact that we are speaking of angles of incidence for which sharp amplitude dips can occur. Figure 15 clearly illustrates that in z-cut quartz we see the following:

(a) Two well defined amplitude dips in $R(\theta)$ vs θ for nearly all azimuthal angles ϕ.

(b) The magnitude of these angles θ_c as a function of ϕ exhibits a 60° periodicity which is an expected characteristic of a hexagonal z-cut quartz slab.

In Fig. 16 we reproduce a sequence of photos illustrating the actual curves of reflected amplitude $R(\theta)$ and phase $\phi(\theta)$ vs θ for a number of azimuthal angles ϕ = 35, 45, 50, and 85°. Note that two distinct amplitude dips are present at all ϕ except ϕ = 50° (also 0° and 110° where only a single well defined dip occurs. It is also clear that the phase curves $\phi(\theta)$ vs θ show anomalies at all azimuthal angles ϕ except ϕ = 50° where a 360° phase shift occurs. Thus, it appears that the anisotropic character of the sample can influence ("trigger") these phase anomalies, but it cannot be entirely responsible for them since these anomalies were also seen in a glass specimen with known isotropic (by our measurements) properties.

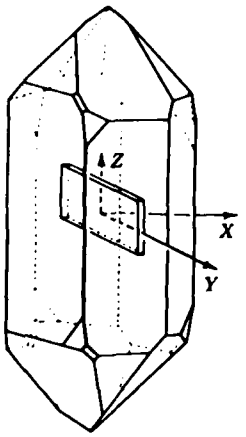

Fig. 14. The x, y and z axes of a quartz crystal. An x-cut slab (perpendicular to x-axis) is illustrated. A z-cut slab would be perpendicular to the z-axis which is also the symmetry axis of the crystal. Note that the x-axis penetrates the line of intersection of two vertical faces of the crystal while the y-axis is perpendicular to these faces. The x and y axes are at 90° to one another and to the z-axis.

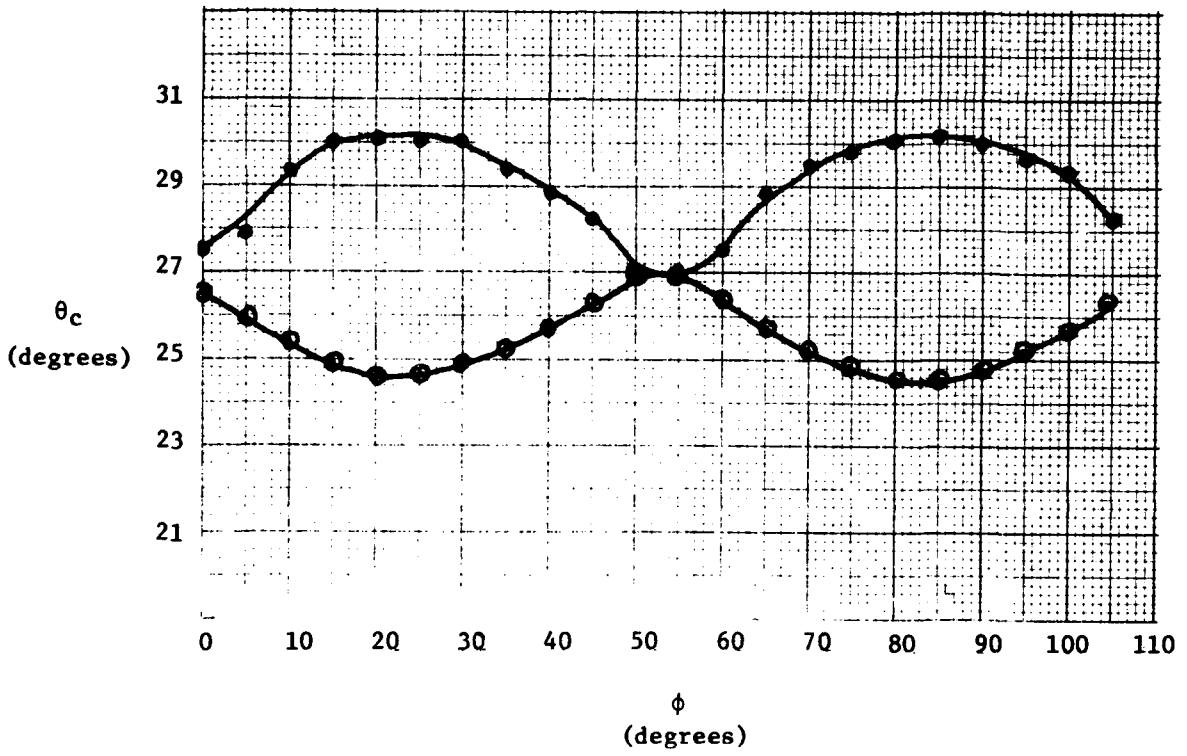

Fig. 15. Critical angles θ_c observed on z-cut quartz versus the azimuthal angle ϕ.

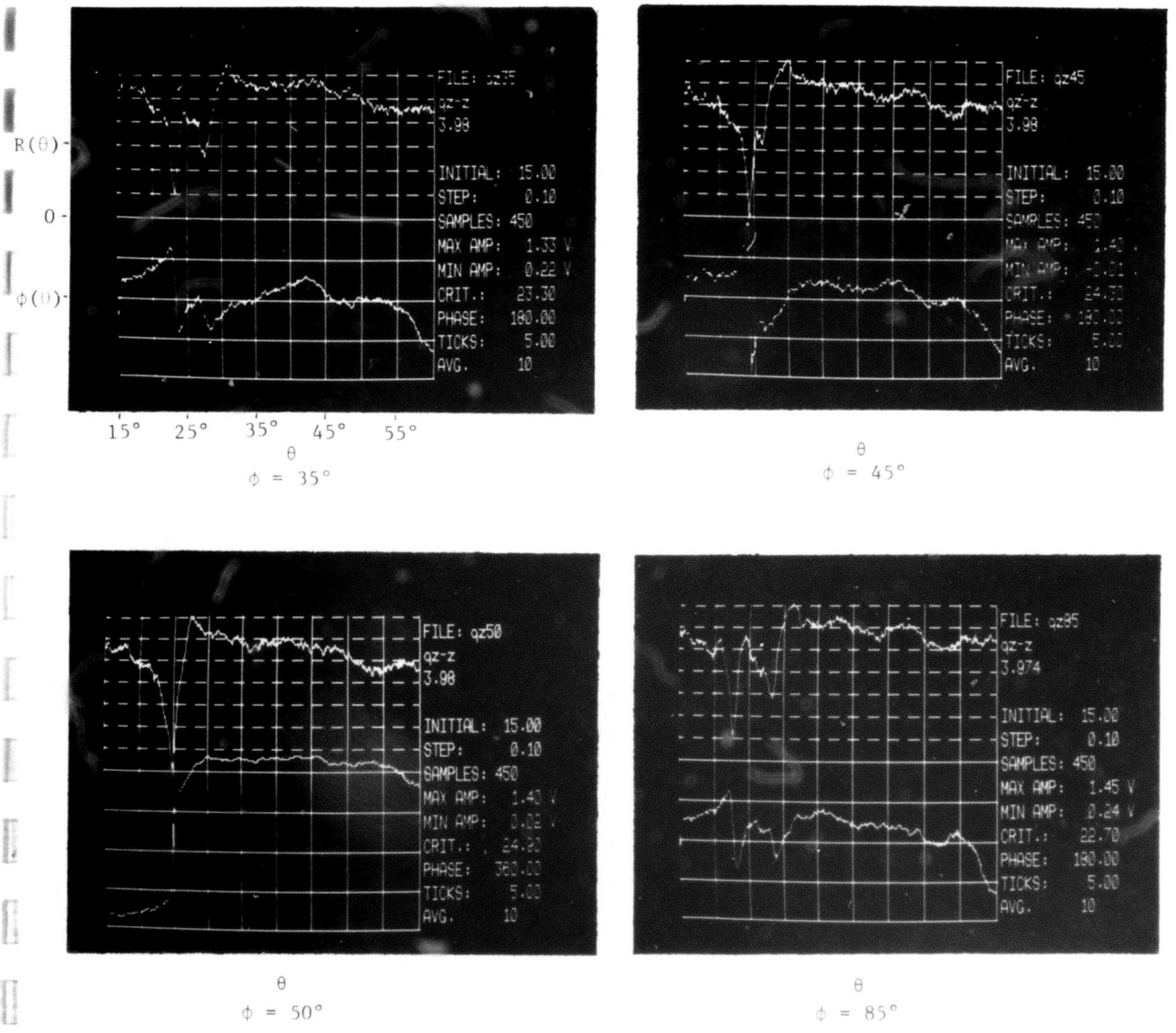

Fig. 16. Amplitude $R(\theta)$ and Phase $\phi(\theta)$ versus the angle of incidence θ for various azimuthal angles ϕ of a z-cut quartz specimen.

As Hennecke points out, quartz should be "multiply refractive" so that five refracted rays should be produced at a water-quartz interface even though there are only three possible bulk waves in quartz. Moreover, he points out that Snell's law cannot be used in calculating velocities from observed critical angles.

We have not as yet reproduced all of the derivation involved to make these conclusions but merely reproduce a figure from Hennecke's paper (see Fig. 17). It is evident that he predicts two very similar critical angle curves (θ_c vs ϕ) to those we observed on z-cut quartz in the same orientation. We have darkened two of Hennecke's five curves. These should be compared with the two curves illustrated in Fig. 15.

Notice that Hennecke's critical angle curves have essentially the same form (θ_c vs ϕ) as our curves but lie roughly 6° below (critical angles are 6° less) the Rayleigh-type critical angle curves we measured (see Fig. 15). This is reasonable in view of the fact that Hennecke is speaking here of the bulk wave quasilongitudinal and quasishear critical angles, and not Rayleigh-type critical angles which are associated with surface waves. Moreover, in optical glass we also saw a similar difference of roughly 6° between the shear mode critical angle and the Rayleigh-type critical angle.

The reasonable agreement between Hennecke's predictions and our observations (especially in view of the fact that Snell's law was invalid in making these predictions) shows that our apparatus is not introducing such effects as multiple dips. In this regard, we cite a final experiment performed on quartz involving a 4 mm diameter "pinhole" placed over the face of our source transducer. Operating at 4 MHz, such an aperture is roughly 10λ across and so does not produce significant diffraction. Such an aperture does eliminate most of the off-axis rays. With this pinhole present, we continue to see the two amplitude dips characteristic of quartz (see Fig. 18). This provides additional conclusive experimental evidence that off-axis rays have little or no effect on our observation.

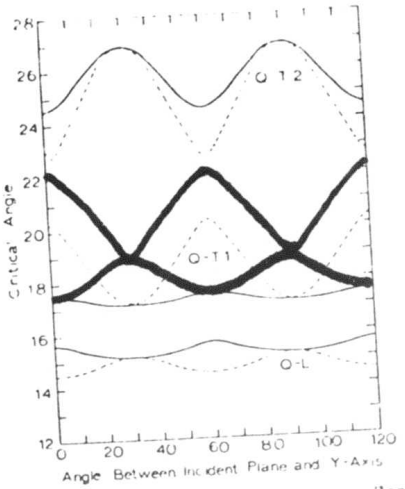

FIG. 1. Critical angle of incident, quasilongitudinal, and quasitransverse modes, versus incident angle for the classical Snell's law (dotted lines) and for the modified law given in the text (solid lines).

Fig. 17. Figure 1 is reproduced from a paper by Hennecke showing theoretically calculated critical angle data for z-cut quartz. We have darkened two of the five curves for comparison with our Fig. 15 experimental data taken on z-cut quartz.

Fig. 18. Z-cut quartz examined using a 4 mm lens stop. The lens stop had little effect on the two critical angles observed in z-cut quartz. This illustrates that off-axis rays are of little importance in locating critical angles accurately.

4.3 Cubic Single Crystals

Following Green[14] and others,[23] we note that cubic single crystals are characterized (in linear approximation) by three second order elastic constants C_{11}, C_{12}, and C_{44}. This situation should be contrasted with the case of isotropic materials where only two second order constants are required.

In Fig. 19 we illustrate the Miller indices for any such crystal with a unit cell of dimension (a).

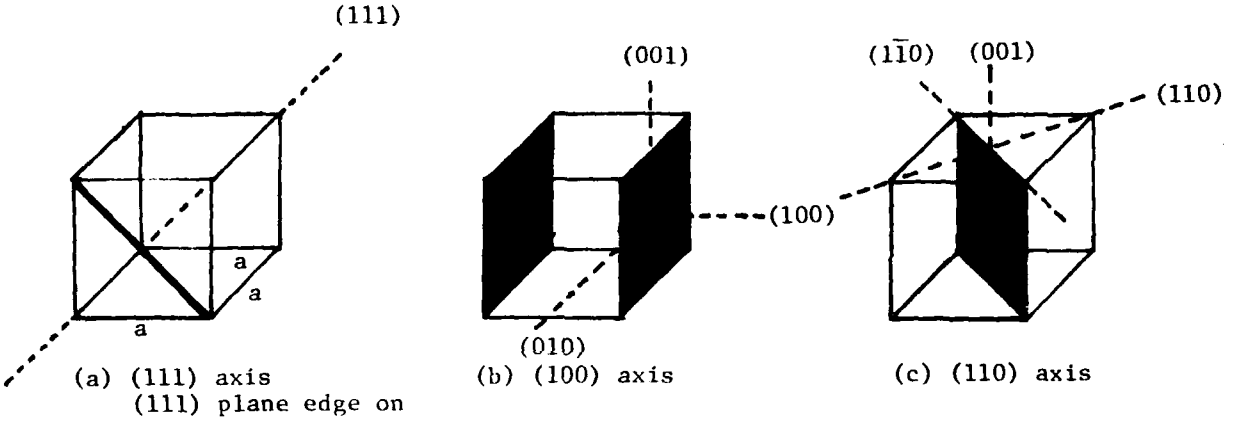

Fig. 19. Miller indices for cubic crystals. The axes are perpendicular to the shaded planes of the same designation. That is, the 100 axis is perpendicular to the 100 plane. Many directions are quivalent in a cubic crystal. For example, the 100 direction is equivalent to the 001 direction or the 010 direction in so far as bulk elastic properties are concerned.

It was shown previously that, in general, there are three bulk waves in any anisotropic material, namely a quasilongitudinal wave and two quasitransverse waves. Along certain axes of the crystal pure mode, longitudinal or transverse waves may propagate. In particular, along the (111) axis of a cubic crystal we find[14]

$$V_1 = ((C_{11} + 2C_{12} + 4C_{44})/3\rho)^{1/2} = V_L \qquad (40)$$

$$V_2 = ((C_{11} - C_{12} + C_{44})/3\rho)^{1/2} = V_{T_1} \qquad (41)$$

and $$V_3 = V_2 = V_{T_2} . \qquad (42)$$

Thus, one pure mode longitudinal wave with group velocity V_1 and one pure mode shear (transverse) wave with velocity $V_2 = V_3$ propagate along (111).

Along the (100) axis, we have

$$V_1 = (C_{11}/\ )^{1/2} = V_L \tag{43}$$

$$V_2 = (C_{44}/\rho)^{1/2} = V_{T_1} \tag{44}$$

and $$V_3 = V_2 = V_{T_2}. \tag{45}$$

Again, there is one pure mode shear wave with velocity $V_2 = V_3 = V_{T_1} = V_{T_2}$ and one pure mode longitudinal wave with velocity $V_1 = V_L$. Note that the velocity of the transverse mode is independent of its polarization along this axis. Finally, along the (110) axis, we have

$$V_1 = ((C_{11} + C_{12} + 2C_{44})/2\rho)^{1/2} = V_L \tag{46}$$

$$V_2 = ((C_{11} - C_{12})/2\rho)^{1/2} = V_{T_1} \tag{47}$$

and $$V_3 = (C_{44}/\rho)^{1/2} = V_{T_2}. \tag{48}$$

That is, we now have two pure mode shear waves with distinct group velocities $V_2 = V_{T_1}$ and $V_3 = V_{T_2}$ and one pure mode longitudinal wave with group velocity $V_1 = V_L$. Note that the shear wave with velocity V_{T_1} is "laterally" polarized along the $(1\bar{1}0)$ direction (see Fig. 19) while the shear wave with velocity V_{T_2} is "vertically" polarized along the (001) direction. In this case, we are imagining that the (001) plane is the surface under study. "Lateral" then refers to polarization parallel to the surface while "vertical" refers to polarization perpendicular to the surface.

Along the pure mode axes, the energy flux vectors are parallel to the wave vectors. Along all other directions, this condition is no longer true. Thus, it is only along these pure mode directions that Snell's law could provide a reasonable description of the refracted waves.

Our copper single crystal was examined by rotating it about the (100) axis (equivalent to the 001 axis) while holding the vertical source-receiver plane of incidence fixed. Thus, during the rotation of the crystal, we encountered the following pure mode axes: (010), (001), and (110) (see Fig. 19(b) and (c)). Equations (43-45) provide the pure mode group velocities for the (010) (equivalently (100),(001)), and Eqs. (46-48) provide the pure mode group velocities for the (110) axis.

Let us compute these pure mode bulk wave velocities for copper, and then calculate their corresponding critical angles using Snell's law. From Truell[16] or Landolt-Bornstein[17] we have the three second order elastic constnat C_{ij} of a copper crystal of density ρ, namely

$$C_{11} = 16.84\ 10^{11} \text{dynes/cm}^2$$
$$C_{12} = 12.14\ 10^{11} \text{dynes/cm}^2 \qquad (49)$$
$$C_{44} = 7.54\ \ 10^{11} \text{dynes/cm}^2$$

and $\rho = 8.94\ \text{gm/cm}^3$.

In Fig. 20 we summarize the results of these velocity calculations.

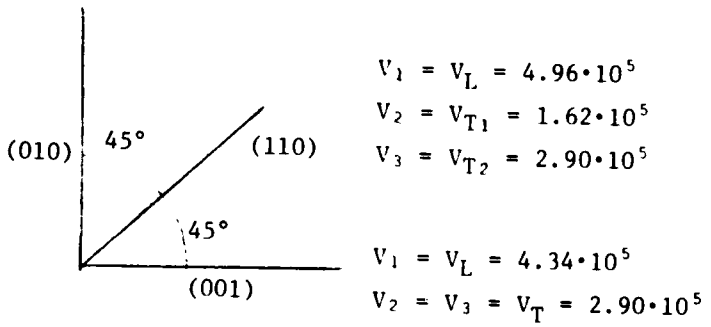

Fig. 20. Calculated group velocities along various pure mode directions in a copper single crystal. V_L = longitudinal velocity and V_T = transverse velocity. All velocities are in units of cm/sec.

Using Snell's law in the real (lossless) form, the bulk wave critical angles θ_c can be estimated from

$$\frac{\sin \theta_c}{V_w} = \frac{1}{V_R} \tag{50}$$

where V_R is the refracted bulk wave velocity in question (V_L or V_T). We have

$$\begin{aligned} \theta_L(001 \text{ or } 010) &= 21.07° \\ \theta_T(001 \text{ or } 010) &= 32.54° \\ \theta_L(110) &= 18.33° \\ \theta_{T_1}(110) &= 74.36° \\ \text{and} \quad \theta_{T_2}(110) &= 32.54° \end{aligned} \tag{51}$$

4.4 Experimental Results on Copper

In Fig. 21 we reproduce our Rayleigh-type surface wave critical angle measurements for a copper single crystal rotated about the (100) axis. The azimuthal angle ϕ was varied in 5° increments and data was taken over a full 360° rotation. In Fig. 22 we illustrate a similar measurement on the same crystal where the azimuthal angle was varied in steps of 2.5° over a 110° range in ϕ.

Two features of these curves are immediately evident: (1) a 90° azimuthal periodicity characteristic of a cubic crystal is present, and (2) there are two critical angles characterized by more or less well defined amplitude dips and phase shifts (see Fig. 24). The fact that there are two critical angles is made more evident in Fig. 22 where greater care was taken in recording indications of a second angle.

The agreement between our measured surface wave critical angles and those calculated theoretically by Diachok[18] is excellent as can be seen from Fig. 23. In this figure we have superimposed

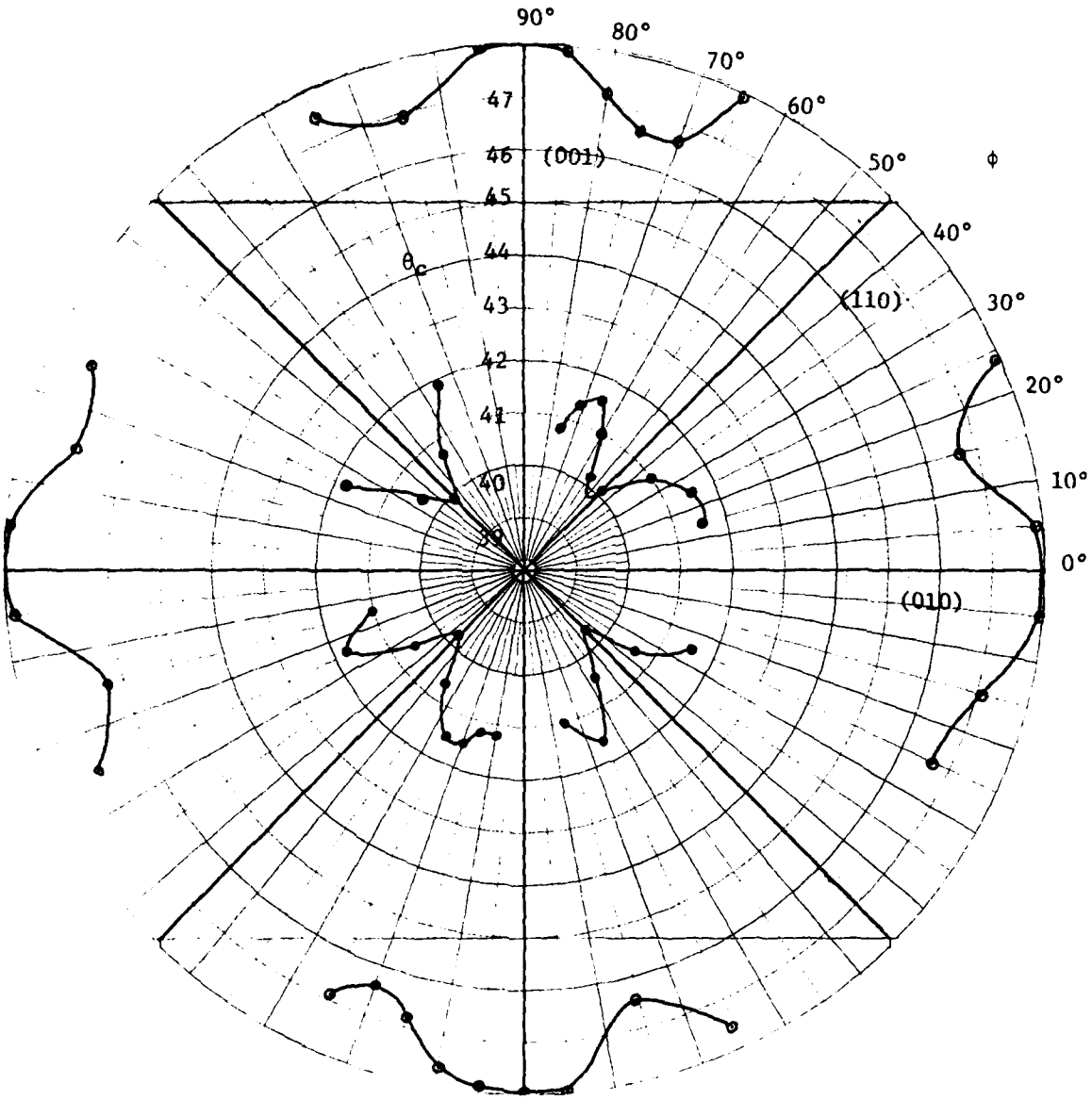

Fig. 21. Rayleigh-type (surface wave) critical angles for a copper single crystal rotated about the (100) axis. The frequency was 3.8 MHz and the two critical angles occur at $\theta_c \approx 41°$ and $\theta_c \simeq 47°$. The azimuthal angle ϕ (angle of rotation about the 100 axis) varied from 0 to 360° and data was taken in steps of $\Delta\phi = 5°$. Pure mode directions (001, 110, and 010) are marked on the figure.

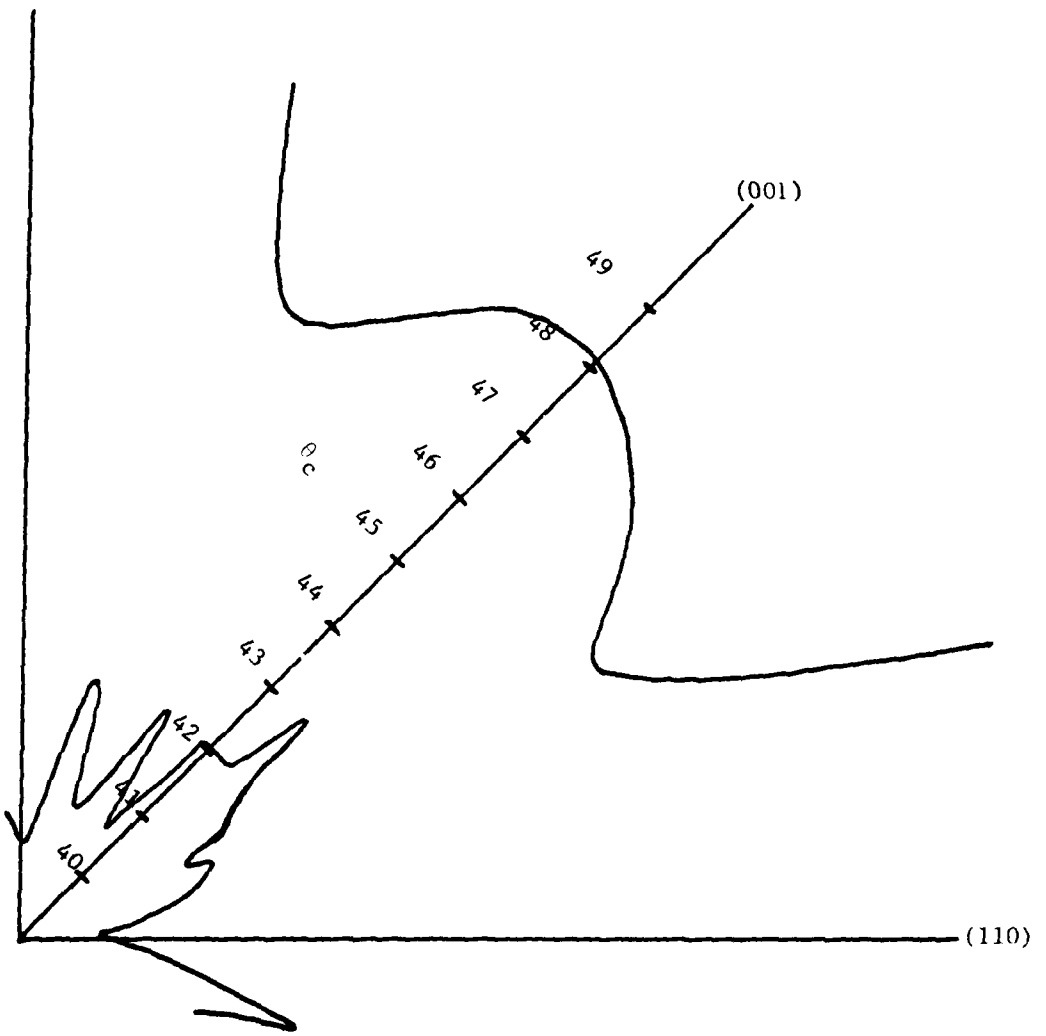

Fig. 22. Same subject as Fig. 21 except $\Delta\phi = 2.5°$ and the range of the data is $\phi = 25°$ to $110°$.

some of our experimental data (taken from Fig. 22) on Diachok's theoretically computed and experimentally verified curves. Note that Diachok employed an entirely different kind of experimental system (a Schlieren optical system) to obtain his results.

In this same figure, we have also included for comparison the pure mode (bulk wave) critical angles for copper given in Eqs. (43-48). Diachok's outer curve (what he calls the "Rayleigh branch") generally lies above the would be curve connecting the points we have labeled T_1. Note, however, that near 45° on Diachok's curve (near the 110 axis) T_1 lies above his calculated curve. We would expect just the reverse, namely T_1 should lie below this Rayleigh-type critical angle. In view of the fact that Diachok has presented no experimental data in this region, we suspect that his theoretically computed curve (solid line) is in error in this region. Diachok's inner curve (what he calls the pseudosurface wave branch) lies above the would be curve connecting the points we have labeled T_2.

The terms "Rayleigh" wave and "pseudosurface" wave, as used here by Diachok, are somewhat misleading. A true Rayleigh wave exists only at a vacuum-solid interface. Moreover, the "shear component" of Rayleigh waves ($\nabla x \Psi$) is always vertical to the free surface.[13,19] Thus, there is some justification for calling the surface wave which propagates along (110) (liquid-solid interface) with vertical polarization a Rayleigh-type surface wave. Note that along (110), the surface wave can be thought of as being closely associated with the T_1 curve since T_1 is also "vertically" polarized (polarization along 001 or 100 perpendicular to the surface). We also note [20] that the effect of liquid loading on the calculated surface wave velocities (along 110) is small. That is, the true Rayleigh wave velocity[21] along this direction is very close to the surface wave velocity along the same direction of a liquid-solid interface.

However, as the azimuthal angle ϕ is changed from the (110) to the (010) axis, the polarization of the bulk shear waves is changing from a "vertically" polarized wave to one of arbitrary

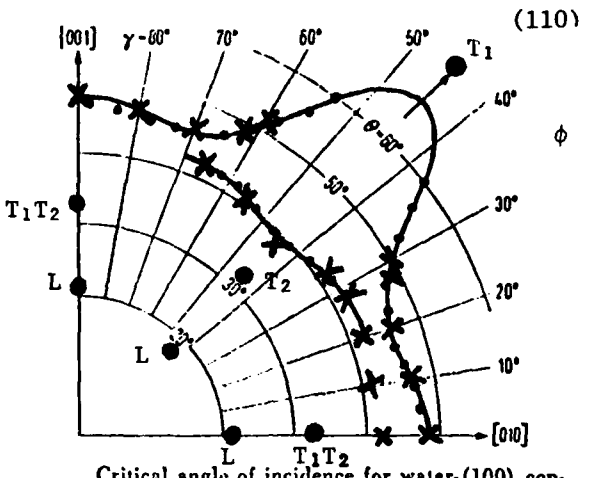

Critical angle of incidence for water-(100) copper surface. Calculated values for RAYLEIGH waves (outer curve) and pseudosurface waves (inner branch) with experimental points.

Fig. 23. Surface wave critical angles for a copper single crystal. Curve reproduced from a paper by Diachok.[18] Diachok's calculations and measurements ——•——•——; pure mode data • • • (L, T_1, T_2); our experimental data ✱—✱—✱—✱ .

polarization. Hence, the close association of Diachok's outer curve with the curve T_1 would no longer be consistent. Similarly, Diachok refers to the inner curve as being the "pseudosurface" wave critical angle presumably because this is closely associated (lies above) with a laterally polarized (polarized along $1\bar{1}0$ for propagation along 110) bulk shear wave.

It would seem more reasonable to think of these surface waves (with liquid loading) as effects completely separate from the "associated" bulk shear waves T_1 and T_2. Thus, the "Rayleigh-type surface wave" is just as much a surface wave as the "pseudosurface" wave. As Plona[22] has pointed out, both types of surface waves show significant vertical polarization.

We have not yet examined these questions thoroughly from a theoretical standpoint (however, Farnell[23] has done so), but experimental evidence on copper seems to support the basic physical similarity of these two surface wave branches. In this regard, consider the data reproduced in Fig. 24. In this figure a series of phase and amplitude curves is reproduced for azimuthal angles $\phi = 57.5°$ to $\phi = 70°$ in steps of $\Delta\phi = 2.5°$. At $\phi = 57.5°$ we are close to the (110) axis (see Fig. 21). There is no evident indication of a second amplitude dip (the Rayleigh-type surface wave branch), but there is a strong amplitude dip at $\theta = 40.4°$. This would fall on Diachok's inner curve (his "pseudosurface" wave branch).

Varying ϕ from $\phi = 57.5°$, we see beginning at about $\phi = 65°$, a stronger indication of a second angle ($\theta \simeq 49.5°$) on the "Rayleigh-branch" while the amplitude dip on the "pseudobranch" is growing weaker. Finally, when we reach $\phi = 70°$, the "pseudobranch" amplitude dip is very weak and the "Rayleigh branch" critical angle ($\theta \simeq 46.6°$) is now very well defined by a sharp amplitude dip and a 360° phase shift. Since the amplitude dips are both very deep at $\phi = 57.5°$ and 70° and since the phase shift is 360° at both of these angles, the surface waves would seem to be very similar physically. It, therefore, seems somewhat artifical to refer to one branch as "Rayleigh" and the other as "pseudo" as Diachok has done. Further theoretical and experimental studies should clarify both the semantics and the physics involved.

Several important conclusions can be drawn from these experimental results regarding our particular experimental arrangement using a focused lens. Both Diachok[18] and Plona[22] have employed broad beam methods to obtain their data. In view of the excellent agreement between our results and Diachok's (on copper single crystals), it is clear that the acoustic lens is not appreciably altering experimental results. Moreover, our technique seems to be more sensitive to a second critical angle. For example, Plona indicates that there are regions (certain ϕ) where he saw no indication of a

second angle. We see such regions also (see Fig. 24), but they are for less wide in ϕ than Plona indicates. Our technique is apparently able to detect a much weaker indication of the presence of a second angle than the Schlieren techniques.

second angle. We see such regions also (see Fig. 24), but they are for less wide in ϕ than Plona indicates. Our technique is apparently able to detect a much weaker indication of the presence of a second angle than the Schlieren techniques.

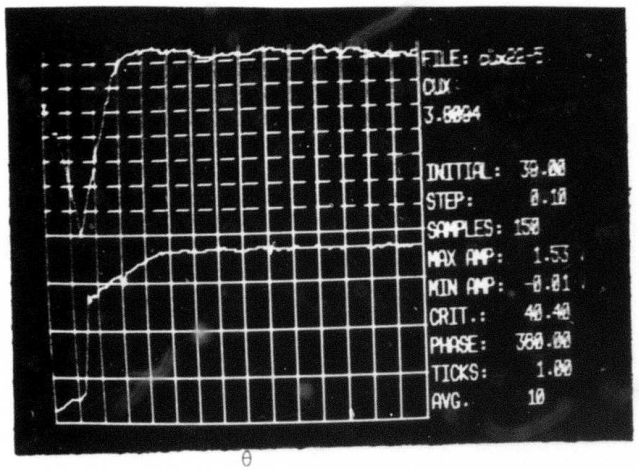

θ

$\phi = 57.5°$

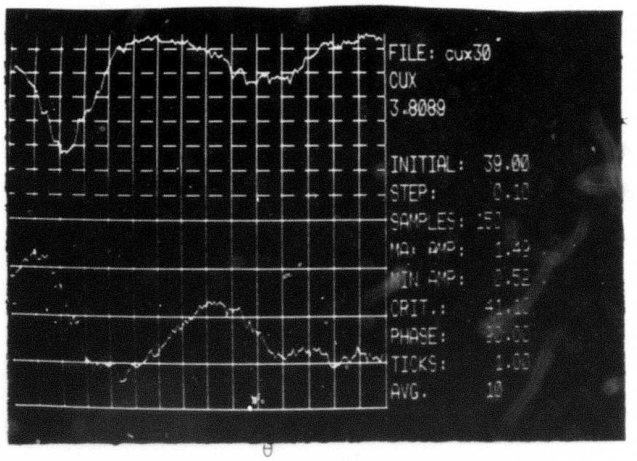

θ

$\phi = 65°$

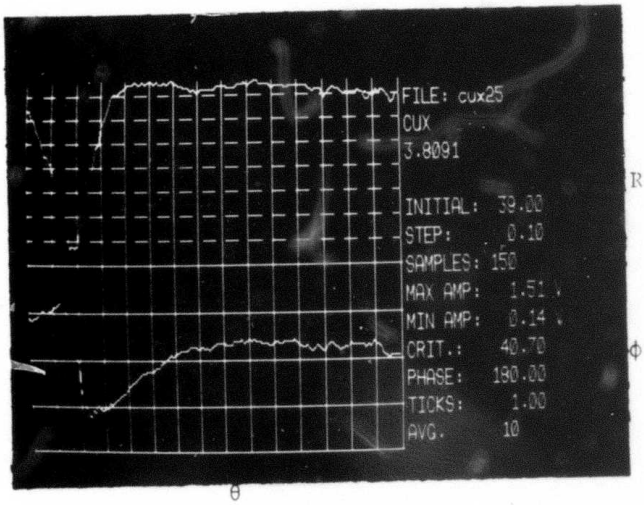

θ

$\phi = 60°$

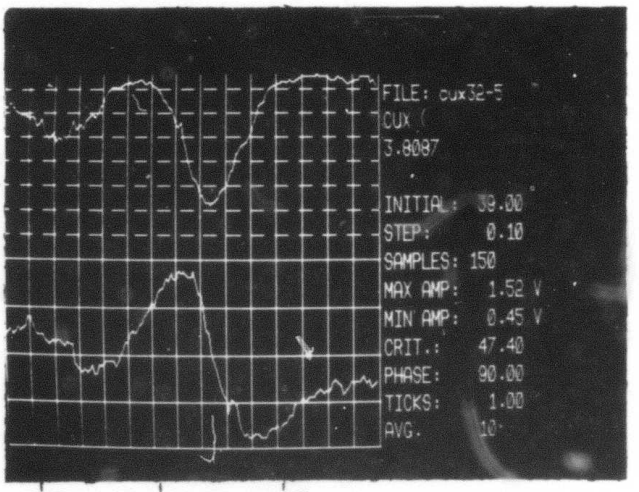

$\phi = 67.5°$

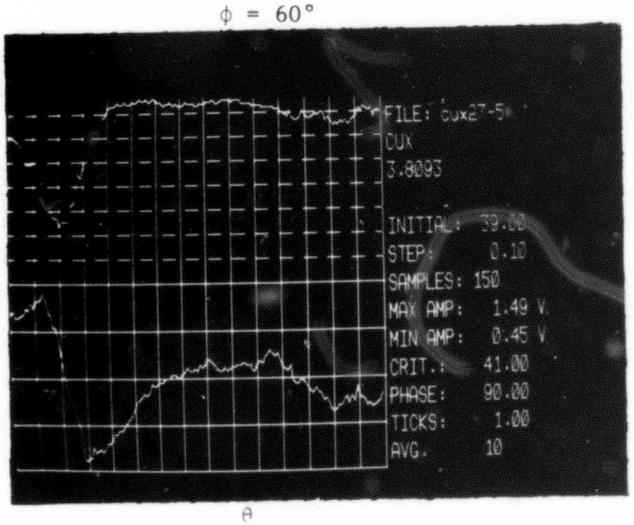

θ

$\phi = 62.5°$

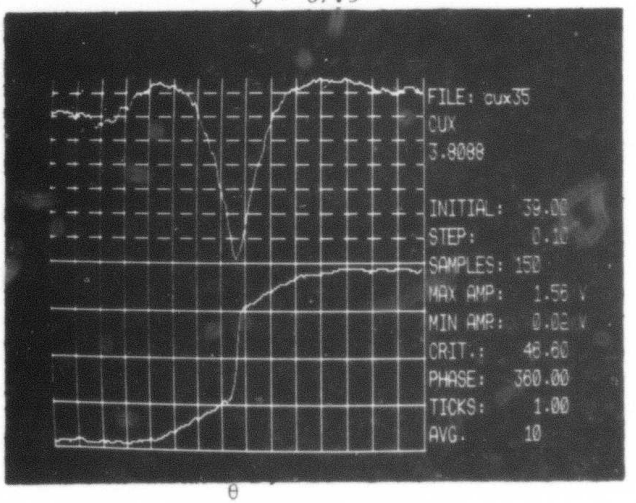

θ

$\phi = 70°$

Fig. 24. Amplitude R(θ) and phase φ(θ) vs θ for different azimuthal angles φ for the copper single crystal (angle of rotation φ about the 100 axis).

5.0 CONCLUSIONS

The foregoing work leads to several conclusions:

(1) Various "anomalies" reported earlier in uncontrolled samples have been seen in controlled single crystals. These effects show periodic angular behavior characteristic of the angular position of the crystals; thereby showing that these anomalies are not spurious results, or results that depend principally upon the particular apparatus used.

(2) Multiple amplitude dips do not occur in isotropic materials, such as glass and many glass-like alloys, but do occur in anisotropic materials. Such anisotropic materials include crystals or polycrystalline alloys with a preferred direction due to rolling alignment, residual stress, or some other anisotropic character. Multiple dips result from the fact that in anisotropic materials the slowness surfaces are very complex. Multiple dips are not a result of finite lens aperture.

(3) Only in certain special cases can critical angle data lead to a complete determination of the elastic constant owing to the fact that Snell's law is generally invalid in anisotropic materials, for example.

(4) Anomalous phase shifts occur in both isotropic and anisotropic materials. The effect is, therefore, not produced by anisotropy though anisotropy appears to influence the effect as demonstrated by data on quartz.

(5) The periodicity in ϕ of these critical angle measurements definitely allows one to orient crystals although the measurement of elastic properties is much more difficult owing to the complexity of the slowness surfaces for anisotropic materials and the resultant additional complexities of a water-solid interface (anisotropic solid).

(6) Our experimental system principally excites waves along the line of intersection of the plane of incidence and the water-solid interface. Off-axis rays appear to have little or no effect on our measurements as evidenced by the agreement between our results on quartz and copper crystals and the work of others.

A number of other interesting observations of a preliminary nature were also made. We have observed, for example, that an angular dependence (ϕ) of the depths of the amplitude curves is present in data on quartz and copper but not on glass (see Figs. 24 and 25). Such amplitude dependence has made it difficult to measure spectral reflectivity for different source intensities as a function of the azimuthal angle owing to the fact that at some azimuthal angles amplitudes saturate our band pass filter. Accordingly, we are in the process of designing an active filter that will allow us to obtain spectral reflectivity curves as a function of ϕ. This information will allow us to assess the extent to which nonlinearities influence our phase measurements. We are also continuing experiments on the other crystals in our possession and will report these results at a later date.

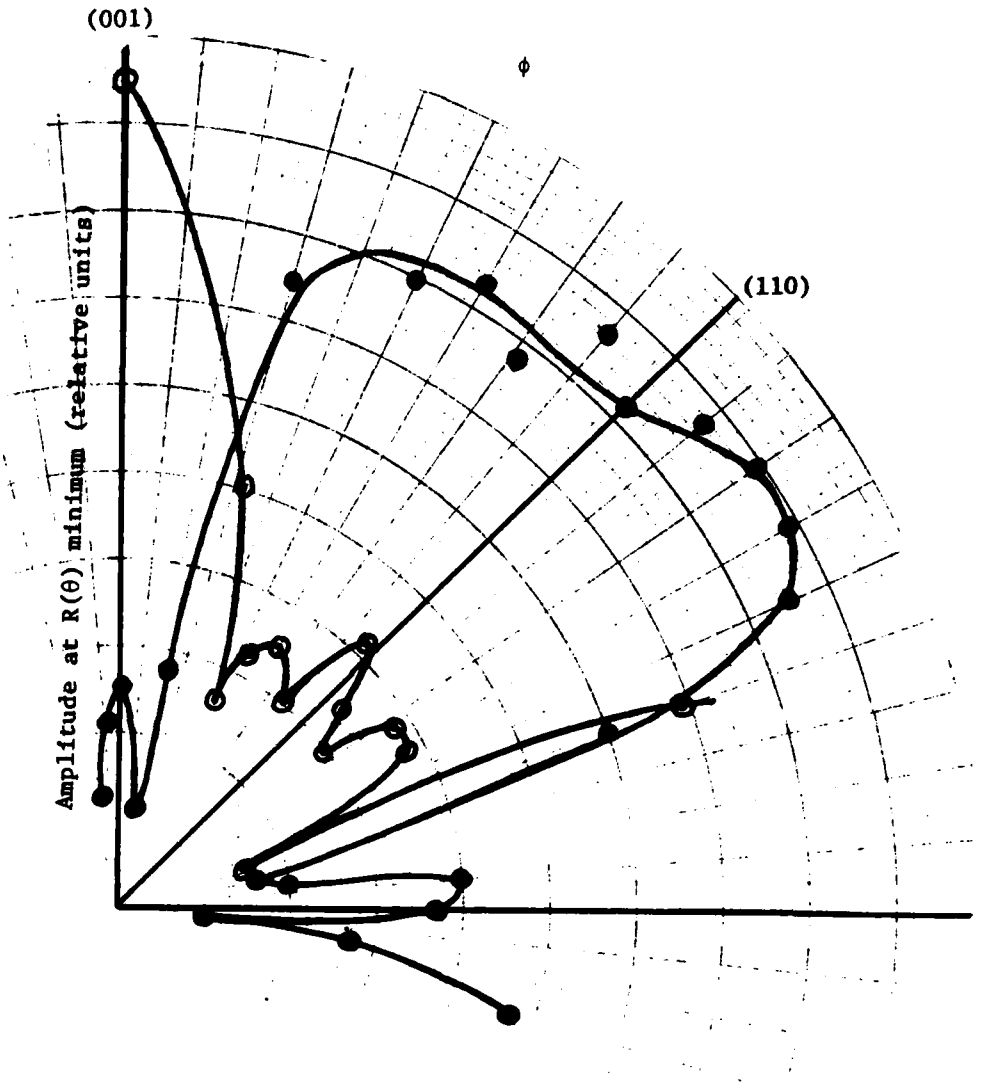

Fig. 25. Observed depths of amplitude minimum at $\theta = \theta$ critical vs azimuthal angles ϕ for a copper single crystal. The angle of rotation ϕ is about the (100) axis of the crystal. The solid circles give the amplitude at the larger of the two critical angles $\theta \simeq 46°$ while the open circle gives the amplitude at the smaller of the two critical angles $\theta \simeq 40°$.

6.0 ACKNOWLEDGMENTS

The authors would like to thank Dr. Howard Greyber (NSF) for suggesting sources of single crystals, and Dr. Hassel Ledbetter (NBS Boulder) for loaning us the five metal single crystals. We would also like to thank Pete Warren (Union Carbide) for giving us crystals of lithium niobate, spinel, and sapphire. The authors thank Yvonne Pipkin for editing and typing this report, and Ray Silta for aid in design and construction of apparatus.

We are especially indebted to Dr. Robert Green (DARPA) and to Captain Steven Wax (Air Force) for several valuable references, and for numerous helpful suggestions.

7.0 REFERENCES

1. H. Überall, "Surface Waves in Acoustics," Physical Acoustics, Vol. X, edited by W. P. Mason and R. N. Thurston, Academic Press, New York (1973).

2. E. G. Henneke II, J. Acoust. Soc. Am. 51, 210-217 (1972).

3. L. D. Rozenberg, "Ultrasonic Focusing Radiators," Sources of High Intensity Ultrasound, edited by L. D. Rozenberg, Plenum Press, New York (1969).

4. B. D. Tartakovskii, "Diffraction of Sound Waves in Convergent Beams," Akust. Zh. 4, 354 (1958).

5. M. Born and E. Wolf, Principles of Optics, 5th edition, Pergamon Press, New York (1975).

6. K. A. Naugol'nykh, "Absorption of Finite-Amplitude Waves," High Intensity Ultrasonic Fields, edited by L. D. Rozenberg, Plenum Press, New York (1971).

7. R. T. Beyer, "Nonlinear Acoustics," Physical Acoustics, Vol. IIB, edited by W. P. Mason, Academic Press, New York (1965).

8. B. P. Hildebrand and G. L. Fitzpatrick, "Investigation of the Rayleigh Critical Angle Phenomenon for the Characterization of Surface Properties, Phase I," Fifth Quarterly Technical Report for AFOSR (June 1982).

9. M. A. Breazeale, "Ultrasonic Studies of the Nonlinear Properties of Solids," Int. J. NDT 4, 149-166 (1972).

10. A. M. Sutin, "Influence of Nonlinear Effects on the Properties of Acoustic Focusing Systems," Sov. Phys. Acoust. 24, (July-Aug 1978).

11. A. L. Van Buren and M. A. Breazeale, "Reflection of Finite-Amplitude Ultrasonic Waves," I Phase Shift, J. Acoust. Soc. Am. 44, 1014-1020 (1968) and II Propagation, J. Acoust. Soc. Am 44, 1021-1027 (1968).

12. M. A. Breazeale, Private Communication.

13. L. D. Landau and E. M. Lifshitz, Theory of Elasticity, Vol. 7, Pergamon Press, New York (1975).

14. Robert E. Green, Jr., Treatise on Materials Science and Technology, Vol. 3, Academic Press, New York (1973).

B. A. Auld, Acoustic Fields and Waves in Solids, Vol. I and II, John Wiley & Sons, New York (1973).

F. E. Borgnis, "Specific Directions of Longitudinal Wave Propagation in Anisotropic Media," Phys. Rev. 98, 1000 (1955).

K. Brugger, "Pure Modes for Elastic Waves in Crystals," J. Appl. Phys. 36, 759 (1963).

15. E. G. Henneke II, "Reflection-Refraction of a Stress Wave at a Plane Boundary Between Anisotropic Media," J. Acoust. Soc. Am. 51, 210-217 (1972).

B. A. Auld, Acoustic Fields and Waves in Solids, Vol. I, John Wiley & Sons, New York (1973).

16. John Truell *et al.*, Ultrasonic Methods in Solid State Physics, Academic Press, New York (1969).

17. Landolt-Börnstein, Numerical Data and Functional Relationships in Science and Technology, Vol. 2, edited by K. H. Hellwege and A. M. Hellwege, Springer-Verlag, New York (1969).

18. Orest I. Diachok et al., "Measurement of Ultrasonic Surface Wave Velocity and Absorptivity on Single-Crystal Copper," Appl. Phys. Lett. 17, 288 (1970).

19. Igor Aleksandrovich Viktorov, Rayleigh and Lamb Waves, Plenum Press, New York (1967).

20. F. R. Rollins, Jr. et al., Appl. Phys. Lett. 12, 236 (1968).

21. The Rayleigh wave velocity C_R is given by $C_R = ((.87+1.12\sigma)/(1+\sigma))C_T$ where σ is Poisson's ratio and C_T is the transverse velocity in the solid (see References 13 and 19).

22. Thomas J. Plona et al., "Ultrasonic Bounded Beam Reflection Effects a Liquid-Anisotropic-Solid Interface," J. Acoust. Soc. Am. 56, 1773 (1974).

23. G. W. Farnell, "Properties of Elastic Surface Waves," Physical Acoustics, Vol. VI, edited by W. P. Mason, Academic Press, New York (1970).